

Document downloaded from:

<http://hdl.handle.net/10251/58367>

This paper must be cited as:

Pereira, A.L.J.; Sans, J. A.; Vilaplana Cerda, R.I.; Gomis, O.; Manjón, F.J.; Rodríguez-Hernández, P.; Muñoz, A.; Popescu, C.; Beltrán, A. (2014). Isostructural Second-Order Phase Transition of b-Bi₂O₃ at High Pressures: An Experimental and Theoretical Study. *Journal of Physical Chemistry C*. 118:23189-23201. doi:10.1021/jp507826j.



The final publication is available at

<http://dx.doi.org/10.1021/jp507826j>

Copyright American Chemical Society

Additional Information

This document is the Accepted Manuscript version of a Published Work that appeared in final form in *Journal of Physical Chemistry C*, copyright © American Chemical Society after peer review and technical editing by the publisher. To access the final edited and published work see <http://dx.doi.org/10.1021/jp507826j>

Document downloaded from:

<http://hdl.handle.net/10251/58367>

This paper must be cited as:

Pereira, A.L.J.; Sans, J. A.; Vilaplana Cerda, R.I.; Gomis, O.; Manjón, F.J.; Rodríguez-Hernández, P.; Muñoz, A.; Popescu, C.; Beltrán, A. (2014). Isostructural Second-Order Phase Transition of b-Bi₂O₃ at High Pressures: An Experimental and Theoretical Study. *Journal of Physical Chemistry C*. 118:23189-23201. doi:10.1021/jp507826j.



The final publication is available at

<http://dx.doi.org/10.1021/jp507826j>

Copyright American Chemical Society

Additional Information

This document is the Accepted Manuscript version of a Published Work that appeared in final form in *Journal of Physical Chemistry C*, copyright © American Chemical Society after peer review and technical editing by the publisher. To access the final edited and published work see <http://dx.doi.org/10.1021/jp507826j>

Isostructural Second-Order Phase Transition of β - Bi_2O_3 at High Pressures: An Experimental and Theoretical Study

A.L.J. Pereira,^{1*} J.A. Sans,¹ R. Vilaplana,² O. Gomis,² F.J. Manjón,¹
P. Rodríguez-Hernández,³ A. Muñoz,³ C. Popescu,⁴ and A. Beltrán⁵

¹ Instituto de Diseño para la Fabricación y Producción Automatizada, MALTA Consolider Team, Universitat Politècnica de València, Camí de Vera s/n, 46022 València (Spain).

² Centro de Tecnologías Físicas: Acústica, Materiales y Astrofísica, MALTA Consolider Team, Universitat Politècnica de València, 46022 València, Spain

³ Departamento de Física, Instituto Univ. de Materiales y Nanotecnología, MALTA Consolider Team, Universidad de La Laguna, La Laguna, Tenerife (Spain)

⁴ CELLS- ALBA Synchrotron Light Source, 08290 Cerdanyola del Valles, Barcelona (Spain)

⁵ Departament de Química Física i Analítica, MALTA Consolider Team, Universitat Jaume I, 12071 Castello (Spain)

Abstract

We report a joint experimental and theoretical study of the structural and vibrational properties of synthetic sphaerobismoite (β - Bi_2O_3) at high pressures where room-temperature angle-dispersive x-ray diffraction and Raman scattering measurements have been complemented with *ab initio* total-energy and lattice dynamics calculations. Striking changes in Raman spectra were observed around 2 GPa while x-ray diffraction measurements evidence no change in the tetragonal symmetry of the compound up to 20 GPa; however, a significant change exists in the compressibility when increasing pressure above 2 GPa. These features have been understood thanks to theoretical calculations, which show that β - Bi_2O_3 undergoes a pressure-induced isostructural phase transition near 2 GPa. In the new isostructural β' phase, the Bi^{3+} and O^{2-} environments become more regular than in the original β phase due to the strong decrease in the activity of the lone electron pair of Bi above 2 GPa. Raman measurements and theoretical calculations provide evidence of the second-order nature of the pressure-induced isostructural transition. Above 20 GPa, XRD

measurements suggest a partial amorphisation of the sample despite Raman measurements still show weak peaks, probably related to a new unknown phase, which still remain up to 27 GPa. On pressure release, the x-ray diffraction patterns and Raman spectra below 2 GPa correspond to elemental Bi-I; thus evidencing a pressure-induced decomposition of the sample during downstroke.

* Corresponding author, Email: andeje@upv.es

KEYWORDS: sphaerobismoite, high-pressure, x-ray diffraction, Raman, ab initio calculations, phase transitions

1. Introduction

A significant increase in the number of published work related to Bi_2O_3 polymorphs in the last twenty years just reflects the industrial, technologic, and scientific importance of this compound. Its peculiar properties such as energy gap, refracting-index, dielectric permittivity and photoconductivity [1-6] have made Bi_2O_3 suitable for a large range of applications, such as optical coating, photovoltaic cells, microwave integrated circuits, fuel cells, oxygen sensor and oxygen pumps [3,7-19]. Furthermore, cation-centered lone electron pairs (LEPs), as those in Pb^{2+} and Bi^{3+} , are tremendously important for applications requiring off-centered polyhedron and their associated dipoles in ferroelectric, piezoelectric and multiferroic materials, actuators, non-linear materials, ionic conductors and high-refractive index materials.

One of the most intriguing properties of bismuth oxide (Bi_2O_3) is the wide variety of its polymorphs. Most of them are common to other 15 group sesquioxides, like As_2O_3 and Sb_2O_3 , and can be understood as derived from a defective fluorite structure by means of symmetry-breaking atomic local distortions [20,21]. The polymorphism of Bi_2O_3 is a complex issue that remains not understood. The most common structure of Bi_2O_3 found in Nature is the monoclinic bismite (α phase; space group (S.G.) $P2_1/c$, No. 14) [22]. However, several other polymorphs can be obtained depending of the preparation or annealing process. Heating α - Bi_2O_3 above 730°C results in the formation of δ - Bi_2O_3 (S.G. $Fm-3m$, No. 225) with cubic fluorite-type structure. On cooling δ - Bi_2O_3 it is possible to

form two intermediate metastable phases at ambient conditions: i) the tetragonal β phase (S.G. $P-42_1c$, No. 114), also known as sphaerobismoite, at ~ 650 °C, and ii) the body-centered cubic γ phase (S.G. $I23$, No. 197) at ~ 640 °C [22,23]. These Bi_2O_3 metastable phases and also new polymorphs can be obtained by using specific synthesis conditions, doping the sample, or if synthesized in nanometric size [24-27]. The metastable triclinic ω - Bi_2O_3 (S.G. $P-1$, No. 2), for example, was observed when a Bi_2O_3 thin film is grown on BeO substrate at 800 °C [28]. Furthermore, another metastable single crystal of orthorhombic ε - Bi_2O_3 (S.G. $Pccn$, No. 56) was obtained by low temperature hydrothermal reaction at 240 °C [29].

Besides temperature, pressure also plays an important role in the observation of new Bi_2O_3 polymorphs. Starting with the α phase, Ghedia *et al.* [30] identified two different metastable polymorphs of Bi_2O_3 at ambient conditions after compressing the sample up to 6 GPa and heating it up to 880 °C for 30 min: trigonal HP- Bi_2O_3 (S.G. $P31c$, No. 159) and monoclinic R- Bi_2O_3 (S.G. $P2_1/c$, No. 14). It must be added that a hexagonal polymorph at high pressure, named HPC- Bi_2O_3 (S.G. $P6_3mc$, No. 186), was recently obtained after pressurizing HP- Bi_2O_3 [31]. On the other hand, at ambient temperature α - Bi_2O_3 experiences a pressure-induced amorphization at 20 GPa [32,33], but it can be recrystallized into the HPC polymorph by annealing the amorphous phase at 20 GPa and 200 °C, as recently reported [34].

In the last years, a considerable amount of work has been devoted to the study of the catalytic properties of Bi_2O_3 at ambient conditions where the metastable β phase has been shown to exhibit better properties than other phases of Bi_2O_3 [1,27,35,36]. The unique tunnel structure of β - Bi_2O_3 (see **Fig. 1**), due to the special orientation of Bi LEPs, is believed to be associated with its excellent photocatalytic activity. These tunnels can provide channels for the transfer of the photogenerated electrons and holes, preventing their excessive recombination and enabling more free carries to participate in the photodecomposition process [37].

In this work, we performed a detailed experimental and theoretical study of the structural and vibrational properties of β - Bi_2O_3 up to 27 GPa by means of angle-dispersive x-ray diffraction (XRD) and Raman scattering (RS) measurements combined with total-energy and lattice dynamics calculations. We have found that β - Bi_2O_3 , unlike α - Bi_2O_3 ,

undergoes a second-order isostructural phase transition (IPT) above 2 GPa which is related to a strong decrease of LEP activity with pressure and that, above 20 GPa undergoes a partial amorphization.

2. Experimental Method

Synthetic β - Bi_2O_3 samples used in the present experiments were purchased from Sigma-Aldrich Inc. with grade purity higher than 99.9%. Room-pressure XRD patterns, performed with a Rigaku Ultima IV x-ray diffractometer with $\text{Cu K}_{\alpha 1} + \text{K}_{\alpha 2}$ (ratio 0.5) wavelength, and RS spectra, performed with a Horiba Jobin Yvon LabRAM HR microspectrometer, allowed us to confirm that the samples contain only a pure β phase. Scanning electron microscopy (SEM) with a JEOL JSM6300 and energy-dispersive x-ray spectroscopy (EDX) measurements with an attached Oxford Instruments detector were also performed to study the morphology and chemical composition of the samples.

In order to perform high-pressure measurements, the sample was loaded together with a 16:3:1 methanol-ethanol-water mixture in a membrane-type diamond anvil cell (MDAC) with diamond culets of 400 μm in diameter. Powder angle-dispersive XRD experiments were performed up to 27 GPa at room temperature in the BL04-MSPD beamline at ALBA synchrotron facility [38]. This beamline is equipped with Kirkpatrick-Baez mirrors to focus the monochromatic beam and a Rayonix CCD detector with a 165 mm diameter active area. We used a wavelength of 0.4246 \AA and the sample-detector distance during the experiment was set to 230 mm. Pressure was determined both by the luminescence of small ruby chips evenly distributed in the pressure chamber [39] and by the equation of state (EOS) of metallic Cu intentionally mixed with the sample. Integration of 2-D diffraction images were performed with FIT2D software [40] while structural analysis was performed with PowderCell [41] and GSAS [42,43] program packages. To obtain information about the LEP activity, we calculated the cation eccentricity with the program IVTON [44] for both experimental and theoretical results.

Unpolarized RS measurements up to 27 GPa were performed with a Horiba Jobin Yvon LabRAM HR microspectrometer equipped with a thermoelectrically-cooled multichannel charge-coupled device detector which allows a spectral resolution better than 2 cm^{-1} . The Raman signal was excited with a HeNe laser (6328 \AA line) with a power of less

than 10 mW and collected in backscattering geometry using an edge filter working in perpendicular configuration and cutting at 100 cm^{-1} . Raman signals down to 50 cm^{-1} can eventually be detected by playing with the angle between the edge filter and the light containing the Raman signal (provided that Rayleigh signal is weak enough and Raman signal is strong enough). Pressure was determined by the ruby luminescence method [39]. The frequency of the Raman-active phonons have been experimentally analyzed by fitting Raman peaks with a Voigt profile fixing the Gaussian linewidth (1.6 cm^{-1}) to the experimental setup resolution [45].

3. Theoretical details

Ab initio total-energy calculations were performed within the framework of density functional theory (DFT) [46]. The VASP package was used to carry out calculations with the pseudopotential method and the projector augmented wave (PAW) scheme, which replace the core electrons and make smoothed pseudovalence wave functions and take into account the full nodal character of the all-electron charge density in the core region [47]. For Bismuth, 15 valence electrons ($5d^{10}6s^24p^3$) were used, whereas for Oxygen, 6 valence electrons ($2s^22p^4$) were used. Highly-converged results were achieved by extending the set of plane waves up to a kinetic energy cutoff of 520 eV. The exchange-correlation energy was taken in the generalized gradient approximation (GGA) with the PBEsol prescription [48]. A dense Monkhorst-Pack grid of k-special points was used to perform integrations along the Brillouin zone (BZ) in order to obtain very well converged energies and forces. At each selected volume, the structures were fully relaxed to their equilibrium configuration through the calculation of the forces on atoms and the stress tensor. In the relaxed configurations, the forces on the atoms are less than 0.006 eV/\AA and deviations of the stress tensor from a diagonal hydrostatic form are less than 0.1 GPa. It should be noted that, within the DFT formalism, the theoretical pressure, $P(V)$, can be determined at the same time as the total energy, $E(V)$, since P (like other derivatives of the energy) can be obtained from the calculated stress.

Lattice-dynamics calculations were performed at the zone centre (Γ point) of the BZ. Highly converged results on forces are required for the calculation of the dynamical matrix using the direct force constant approach [49]. The construction of the dynamical

matrix at the Γ point of the BZ involves separate calculations of the forces in which a fixed displacement from the equilibrium configuration of the atoms within the primitive cell is considered. The number of such independent displacements in the analysed structures is reduced due to crystal symmetry. Diagonalization of the dynamical matrix provides the normal mode frequencies. Moreover, these calculations allow one to identify the symmetry and eigenvectors of the vibrational modes in each structure at the Γ point.

4. Results

4.1 Characterization of β -Bi₂O₃ at ambient pressure

The tetragonal structure of β -Bi₂O₃ at room pressure has a distorted defect-fluorite structure with one Bi atom located at $8e$ Wyckoff site and two O atoms located at $8e$ and $4d$ Wyckoff sites. In this structure, Bi is six-fold coordinated and the polyhedron surrounding Bi resembles a distorted pyramid with Bi-O bond lengths varying from 2.09 to 2.72 Å (see **Fig. 1(a)**). Curiously, Bi and O atoms are arranged in slightly distorted sheets parallel to the plane (001) as in a layered material (see **Fig. 1(b)**). The formation of atomic layers seems to be a common feature in many Bi-related compounds, like the polymorphs α -Bi₂O₃ and HPC-Bi₂O₃ [33], Bi₂S₃ [50] and some recently discovered topological insulators based on Bi, like Bi₂Se₃, Bi₂Te₃ and Bi₄Te₃. As it can be observed in **Fig. 1(b)**, the atomic configuration of β -Bi₂O₃ structure is strongly asymmetric and results in the formation of empty tunnels due to the intersection of the Bi LEPs in certain locations.

The crystalline structure of the studied sample was characterized at room conditions by means of XRD, RS, EDX, and SEM measurements. **Figure 2(a)** and **2(b)** show the XRD pattern and RS spectrum obtained for β -Bi₂O₃ at room pressure, respectively. The XRD pattern agrees well with the JCPDS data card No. 78-1793. The measured lattice parameters at 1 atm are: $a = 7.74002(5)$ Å and $c = 5.62671(7)$ Å, yielding a unit-cell volume $V_0 = 337.08(5)$ Å³. These values are in agreement with our *ab initio* calculations for the β phase, where we have found that V_0 is 0.6% underestimated in comparison with the experimental values. These values are also in good agreement with those previously found in the literature [51].

As regards the lattice dynamics of β -Bi₂O₃, there are four formula units in the primitive cell and therefore there are 60 normal modes of vibration at zone center whose mechanical decomposition is:

$$\Gamma = 7 A_1(\text{R}) + 7 A_2 + 7 B_1(\text{R}) + 7 B_2(\text{R,IR}) + 16 E(\text{R,IR})$$

where E modes are doubly degenerated, A₂ modes are silent, B₁ modes are Raman-active (R) and B₂ and E are polar modes which are both Raman and infrared-active (IR). Therefore, there are thirty seven Raman-active modes ($\Gamma_{\text{Raman}} = 7 A_1 + 7 B_1 + 7 B_2 + 16 E$), twenty-one infrared-active (IR) modes ($\Gamma_{\text{IR}} = 6 B_2 + 15 E$) and two acoustic modes ($\Gamma_{\text{acoustic}} = B_2 + E$). The polar modes also show a transversal optic-longitudinal optic (TO-LO) splitting; however, such a splitting is expected to be rather small because of the small ionicity of Bi₂O₃ [33].

As can be observed in **Fig. 2(b)**, RS measurements at ambient pressure show four intense peaks at ~ 90 , ~ 125 , 313 and 465 cm⁻¹, and seven less intense peaks. The large number of Raman-active modes and the broadening of many of them make some modes hard to identify at room conditions because there are several close Raman peaks which overlap. In the next section we will show that other peaks can be observed because of the splitting of the Raman bands at high pressures. In particular, we have observed that the intense peaks at ~ 90 and ~ 125 cm⁻¹ are composed by pairs of modes at 89+94 cm⁻¹ and 124+127 cm⁻¹, respectively. Taking into account these considerations, it was possible to identify a total of fourteen Raman-active modes at room conditions. The positions of these peaks are listed in **Table III** for comparison with the theoretical calculations and the results of previous works. As it can be observed in **Table III**, our experimental and theoretical frequencies for the Raman-active modes at 1 atm are in good agreement and also agree with those already reported in the literature [52].

SEM images of our β -Bi₂O₃ powders (**Fig. 2(c)**) prove that they are composed of aggregated submicron particles with average size around 200 nm. In this respect, it is known that β -Bi₂O₃ is a metastable phase observed when the δ phase is cooled below 650 °C. The synthesis of metastable β -Bi₂O₃ as bulk material is based on the use of specific precursors, or as thin films, nanowires, nanoflakes, or nanospheres [27,35,36,51,53-55]. In

our case, the fact that the samples have a sub-micrometric particle size, promote the stabilization of the β phase at ambient conditions. In order to observe the elements present in the sample, EDX analysis was performed (see **Fig. 2(d)**). No other elements, apart from Bi and O were detected after a cleaning procedure where C from the graphite film, which is needed to perform EDX measurements, and Be from the equipment window are removed. This indicates that no other element was used in the sample preparation in order to stabilize the β phase. Note that the β phase has been previously reported to be stabilized by intentionally substituting Bi with a lighter element [56] and by doping the α phase with ZrO_2 [57].

4.2 XRD measurements under pressure

Figure 3 shows the angle-dispersive XRD patterns of β - Bi_2O_3 with increasing pressure up to 27.2 GPa. We performed Rietveld refinement to the XRD patterns recorded up to 12 GPa using the tetragonal $P-42_1c$ structure of β - Bi_2O_3 . In this range of pressure, all diffraction peaks shift to larger angles on increasing pressure, which is coherent with the decrease of interplanar distances with pressure, and some weak peaks disappear already at 2 GPa while a diffraction peak appears at $\sim 8.5^\circ$ at 5.1 GPa. This peak is not due to β - Bi_2O_3 and we believe that it is related to some impurities unintentionally loaded inside the MDAC. At 16.8 GPa, the XRD pattern of β - Bi_2O_3 presents an important intensity loss and peak broadening which develops further on increasing pressure. Above 20 GPa, the XRD patterns only show broad bands besides the Cu diffraction peaks, indicating a possible amorphisation of the sample. On decrease of pressure, the diffraction pattern obtained at 1.3 GPa shows peaks that correspond to the Bi-I structure (S.G. $R-3m$, No. 166) (see top of **Fig. 3**) [58], suggesting that the sample undergo a decomposition process during downstroke which will be further commented in the next section when discussing Raman spectra. The broad band observed in the pattern at 1.3 GPa on downstroke near to 8° seems to correspond to the amorphous structure already observed at high pressure.

XRD data analysis allows us to estimate the pressure dependence of the lattice parameters (a, c) of β - Bi_2O_3 (see **Fig. 4(a)**). The axial compressibility, defined as $\kappa_x = -\frac{1}{x} \frac{\partial x}{\partial P}$, and obtained from a fit of experimental data to a modified Murnaghan EOS [59] are

reported in **Table II** for a and c axes. We have estimated the axial compressibilities at zero pressure using data in three different pressure ranges: 0-12 GPa, 0-2 GPa, and 2-12 GPa. For the case of the a -axis it is observed a strong decrease of the experimental axial compressibility at zero pressure κ_a when comparing the value obtained in the range 0-2 GPa ($\kappa_a = 13.5 \cdot 10^{-3} \text{ GPa}^{-1}$) with that obtained in the range 2-12 GPa ($\kappa_a = 4.1 \cdot 10^{-3} \text{ GPa}^{-1}$). Our calculations are in agreement with this result. On the other hand, the evolution of the c -axis with pressure is not prone to vary; i.e., and the experimental values of the axial compressibility for the c -axis κ_c obtained in the range 0-2 GPa and 2-12 GPa are very similar (see **Table II**). The anomalous change in the compressibility of the a lattice parameter is clearly exposed when we plot the evolution of the c/a ratio with pressure (**Fig. 4(b)**). Experimental c/a shows a steep increase from 0.727 at 1 atm to 0.731 near 2 GPa and then a slow decrease to 0.723 at 12 GPa, which is rather well reproduced by our theoretical calculations (see **Fig. 4(b)**). The strong decrease in compressibility of the a lattice parameter and the change of sign in the slope of the c/a ratio near 2 GPa clearly indicates the existence of an IPT from the β phase towards a new phase (hereafter noted as β') in β - Bi_2O_3 .

Figure 5 shows the experimental and theoretical pressure dependence of the unit-cell volume of β - Bi_2O_3 up to 12 GPa. The P - V data are fitted using a 2nd-order and 3rd-order Birch-Murnaghan (BM) EOS to obtain the zero pressure volume, V_0 , bulk modulus, B_0 , and its pressure derivative, B_0' , which are summarized in **Table II** and compared with the values obtained from our theoretical calculations. As it can be observed in **Table II**, the fit of all data using the 3rd-order BM EOS leads to an unusual large value for B_0' both to experimental and theoretical results. This large derivative ($B_0' > 10$) indicates a strong increase in the B_0 value of β - Bi_2O_3 with increasing pressure, especially above 2 GPa and suggests a rather unusual compression of the β phase. Following the previous results, it has more physical meaning to fit the P - V data taking data points from two different pressure ranges: i) 0-2 GPa (β phase), and ii) 2-12 GPa (β' phase). The results of the EOS for both experimental and theoretical data fitted to 2nd-order and 3rd-order BM EOS in these two ranges are summarized in **Table II**. We note that by fitting EOS to both experimental and theoretical data in two separated pressure ranges, we achieved more reasonable results for B_0 and B_0' . In the case our experimental data, for β - Bi_2O_3 from 1 atm to 2 GPa, we get $B_0 =$

38(1) GPa when we constrain B_0' to 4. A fit using a 3rd-order BM EOS, yields $B_0 = 34(5)$ GPa and $B_0' = 8(5)$. For β' -Bi₂O₃ above 2 GPa, the material becomes rather more resistant to the compression with $B_0 = 77(2)$ GPa when we constrain $B_0' = 4$, or $B_0 = 55(17)$ GPa with $B_0' = 8(4)$ when data are fitted to a 3rd-order BM EOS. It can be noted that when we separate the P - V curve into two zones, the uncertainties in the determination of B_0' from the experimental results are relatively high when compared to the theoretical results. This is related to the limited number of experimental points that we have in both pressure zones. Nevertheless, the values of B_0' obtained from the experiment when we have divided all data into two pressure ranges presents more consistent values ($B_0' < 10$), despite being relatively high when compared to ionic-covalent solids, and are in good agreement with the theoretical results (see **Table II**).

It is noteworthy the higher compressibility of tetragonal β -Bi₂O₃ ($B_0 = 38(1)$ GPa) than monoclinic α -Bi₂O₃ ($B_0 = 79.2(3)$ GPa [33]). The bulk modulus of β -Bi₂O₃ is comparable to those of molecular solids like senarmonite, the most common phase of Sb₂O₃ [60], and likely of arsenolite, the most common phase of As₂O₃. The presence of a second-order IPT in tetragonal β -Bi₂O₃, i.e., a phase transition without any change in the symmetry of the crystalline lattice and no discontinuity in the volume [61], is similar to those already observed in Bi₂S₃ [50], Sb₂O₃ [60], and BiMn₂O₅ [62].

Rietveld refinements performed at 0.6 GPa yield residuals of $R_p = 0.7\%$ and $R_{wp} = 1.1\%$ while those performed at 12 GPa yielded $R_p = 1.8\%$ and $R_{wp} = 2.7\%$. In the β phase, one Bi and one O occupy $8e$ (x,y,z) Wyckoff sites while the other O occupies a $4d$ ($0,1/2,z$) Wyckoff site, as previously commented. Since O has a smaller x-ray scattering cross section than Bi, it is difficult to obtain accurately the four atomic coordinates corresponding to the two different oxygen atoms by Rietveld refinement of the XRD patterns at high pressures. Therefore, the atomic coordinates of the oxygen atoms were refined just at 1 atm and constrained in the following refinements up to 2 GPa. On the other hand, the Bi fractional coordinates and unit-cell parameters were refined up to 2 GPa. From 2 GPa, we observed a significant change in the evolution of the lattice parameters with pressure, but we did not obtain coherent values in the refinement of the Bi position. For this reason, from 2 to 12 GPa we constrained the values of atomic position obtained by our theoretical calculations at 2.3 GPa for the Bi and the two O. The atomic coordinates obtained by the

Rietveld refinement at 1 atm and the theoretical ones at 1 atm and at 2.3 GPa (to perform the refinements in the β' phase) are presented in **Table I**. The values obtained at 1 atm are in good agreement with the results obtained by neutron diffraction [51] and with the values obtained by our theoretical calculations.

Figure 6 shows the calculated evolution of the atomic coordinates of Bi ($8e$), O1 ($8e$) and O2 ($4d$) atoms with increasing pressure. It is noteworthy the clear change in the evolution of the atomic coordinates of all atoms near to 2 GPa. For Bi, the x_{Bi} coordinate, initially at 0.021, decreases sharply to zero at 2 GPa and becomes independent on pressure above 2 GPa (see **Fig. 6(a)**). The evolution of the y_{Bi} and z_{Bi} position with pressure, initially near 0.26 and 0.23, respectively, also present a decrease (but less intense) up to 2 GPa and for the case of y_{Bi} remains almost constant above this pressure. In this respect, we want to stress that the refinement of the experimental Bi position performed up to 2 GPa matches very well with our theoretical results (**Fig. 6(a)**). For O1, the z_{O1} coordinate decreases from 0.034 to zero at 2 GPa and becomes independent on pressure above 2 GPa, while the x_{O1} and y_{O1} coordinates tend to a single value above 2 GPa (**Fig. 6(b)**). Finally, the z_{O2} coordinate shows a change in the slope at 2 GPa (**Fig. 6(c)**). Note that the experimental and theoretical z_{O2} coordinate at 1 atm shows a slightly larger deviation than other coordinates; however, our experimental value (0.38) is not very different from that previously reported from neutron diffraction experiments (0.39) [51]. The above commented changes clearly show that some of the Bi and O coordinates tend to fixed values at 2 GPa; thus indicating an increase of the symmetry of all occupied Wyckoff sites and, consequently, of the compound above 2 GPa.

The increase of symmetry on going from β - Bi_2O_3 to β' - Bi_2O_3 can be clearly seen in **Fig. 7(a)** which shows the theoretical evolution of the Bi-O distances in the BiO_6 polyhedron. At 1 atm, the BiO_6 polyhedron is highly asymmetric with six different Bi-O distances which suggests the existence of a localized and very active LEP. On increasing pressure, the Bi-O1(2) distance decreases and the Bi-O1(1) distance increases so that these two distances coincide at 2 GPa, having both a similar decrease with pressure above 2 GPa (**Fig. 7(a)**). A similar behavior can also be observed between the Bi-O1(4) and Bi-O1(3) distances (see **Fig. 7(a)**). On the other hand, the Bi-O2 distances do not present such a drastic behavior with pressure: the Bi-O2(1) distance presents a smooth decrease and the

Bi-O2(2) distance presents an almost insignificant decrease (see **Fig. 7(a)**). In summary, the BiO₆ polyhedron above 2 GPa exhibits basically only three different Bi-O distances, two of which do not change significantly with the pressure increase (see **Fig. 7(a)**). These results indicate that the pressure increase up to 2 GPa induces a relatively fast regularization of the polyhedron which forms the β -Bi₂O₃ structure while the variation is very smooth above 2 GPa; i.e., the pressure dependence of the Bi-O distances again shows the increase of symmetry of the tetragonal structure of β -Bi₂O₃ on increasing pressure.

The key to understand the compression mechanism and the IPT in β -Bi₂O₃ resides in the understanding of the LEP activity of Bi³⁺ ion, which is one major cause of the distortion in coordination polyhedral of LEP-bearing compounds [31,63]. Hence, studying the evolution of the polyhedral distortion with pressure can give us important information about the LEP activity [63]. The polyhedral distortion of the Bi³⁺ environment can be monitored by the displacement of the cation relative to the centroid of the coordination polyhedron, being the centroid the point which comes closest to the condition of being equidistant to all the coordinated ligands. The displacement of the cation relative to this point divided by the average distance of the cation to ligands is called the eccentricity [63,64]. The eccentricity is an important measure for the stereochemical LEP effect (when becomes equal to zero the LEP ceases to exist). The pressure dependence of Bi eccentricity in β -Bi₂O₃ is plotted in **Fig. 7(b)**. It can be observed that the experimental eccentricity of Bi³⁺ in β -Bi₂O₃ obtained at 1 atm (0.26) is in good agreement with our theoretical calculation (0.22) and also agrees with the eccentricity of Bi³⁺ in Bi₂Ga₄O₉ (0.28) at 1 atm [63]. For the sake of comparison, we have also calculated the eccentricity of the two unequivalent Bi³⁺ atoms in α -Bi₂O₃ at 1 atm. Both eccentricities show to be lower (0.16 for Bi1 and 0.17 for Bi2) than that of Bi³⁺ in β -Bi₂O₃. The Bi³⁺ eccentricity in the β -Bi₂O₃ also is higher than in the Bi₂S₃ (0.14 for Bi1 and 0.16 for Bi2) [66], that also shows a pressure-induced IPT [50], PbBi₂S₄ (between 0.08 and 0.12) [67], and Pb₃Bi₂S₆ (between 0.04 and 0.10) [68], thus suggesting that the value of cation eccentricity depends not only on the structure but also on the anion.

As regards the pressure dependence of experimental (theoretical) eccentricity of Bi³⁺ in β -Bi₂O₃, it shows a steep decrease from 0.26 (0.22) at 1 atm to 0.17 at 2 GPa, both experimentally and theoretically, and our calculations show a smooth decrease above 2 GPa

from 0.17 till 0.13 at 12 GPa. Experimental eccentricity couldn't be calculated at pressures higher than 2 GPa because we did not obtain coherent values in the refinement of the atomic positions above that pressure as previously commented. The notable decrease of the pressure coefficient of calculated eccentricity (**Fig. 7(b)**) is consistent with the more regular BiO_6 polyhedron in the β' phase (above 2 GPa) than in the β phase (below 2 GPa). Extrapolations of the tendencies found in **Fig. 7(b)** show that eccentricity will become zero at ~ 10 GPa in the β phase and at ~ 90 GPa in the β' phase. These results clearly indicate that the LEP remains active in the β' phase after the second-order IPT has taken place in β - Bi_2O_3 . This result indicates that the LEP activity decreases but does not disappear. A pronounced LEP activity at high pressure also occurs in a number of other compounds like HP- Bi_2O_3 [31], $\text{Bi}_2\text{Ga}_4\text{O}_9$ [63], Bi_2S_3 , $\text{Cu}_4\text{Bi}_5\text{S}_{10}$ [65,66], PbBi_2S_4 [67], $\text{Pb}_6\text{Bi}_2\text{S}_9$ [69], and $\text{Bi}_2\text{Fe}_4\text{O}_9$ [70]. In summary, it can be concluded that despite the role of the cation LEP in producing distorted polyhedra and in pressure-induced phase transitions is still a matter of debate [65,71], the reported studies seem to suggest that LEP activity decreases with the increase of anion mass and with the increase of pressure. The reduction of the LEP activity results in a more centered position for the cation in the polyhedral units and in particular, it can lead to new isostructural phases at high pressures, as it occurs in β - Bi_2O_3 , Bi_2S_3 and α - Sb_2O_3 .

4.3. Raman scattering measurements under pressure

Figure 8 shows the Raman spectra of β - Bi_2O_3 at selected pressures up to 27 GPa. The large number of Raman-active modes and the broadening of many of them make some modes hard to identify at room conditions because there are several close Raman peaks which overlap. This is similar to the case of α - Bi_2O_3 already commented in some references [34,72]. Three weak peaks at 30, 161, and 197 cm^{-1} disappear with increasing pressure before reaching 2 GPa. This result supports the analysis made in the previous section. However, the pressure increase allows a clear observation of two new peaks that were overlapped with more intense peaks, near 90 and 125 cm^{-1} at 1 atm, and another weak peak that was detected at ~ 500 cm^{-1} in the β' phase above 2 GPa. Above 15 GPa some new peaks develop while peaks of β' phase have an important intensity decrease. This decrease is severe above 19 GPa and the appearance of six new weak peaks near to 100, 130, 220,

420, 470, and 500 cm^{-1} at 19.1 GPa and near to 120 cm^{-1} at 20.3 GPa suggest the onset of a phase transition to a new phase, hereafter noted χ phase (see **Fig. 8**). At 21.9 GPa, the Raman peaks of the β' phase completely lose their shapes and intensities and only broad bands are observed, which is consistent with a partial amorphisation of the material as observed by XRD measurements. At 21.9 GPa, new peaks appear near to 150, 200, 295, and 320 cm^{-1} which could correspond to the χ phase phase; however, amorphization prevented the identification of this new phase from our XRD measurements. All the new peaks developed above 15 GPa and at 21.9 GPa remain overlapped with the amorphous bands up to 27 GPa. At this pressure, is possible to observe another small band near 380 cm^{-1} (**Fig. 8**). On pressure decrease, we observed a RS spectrum consisting mainly of broad bands coming from the amorphous phase. However, on decreasing pressure below 2 GPa the RS spectrum exhibits new peaks which further develop under strong laser irradiation (see two top spectra in **Fig. 8**) and these RS spectra are completely different than that of the original sample. We have checked that this spectrum corresponds to the pure Bi-I structure [73]; therefore, our RS measurements agree with our XRD data and reinforce the idea that β - Bi_2O_3 exhibits a decomposition on decreasing pressure from the amorphous state.

Regarding the dissociation of the sample, we must stress that the new peaks observed above 15 GPa cannot be associated to the high pressure structure of the Bi [58] because it has a cubic bcc structure and has no Raman-active modes . Furthermore, they cannot be attributed to solid ϵ - O_2 since none of the bands of this phase [74,75], including the vibron mode above 1600 cm^{-1} , has been observed in β - Bi_2O_3 above 15 GPa. Therefore, at present we do not know the origin of the new Raman bands that appear above 15 GPa and which we tentatively attribute to the χ phase of Bi_2O_3 ; but we can conclude that on upstroke there is an amorphization and not a dissociation of β - Bi_2O_3 .

Figure 9 shows the experimental (symbols) and theoretical (solid lines) Raman-mode frequencies of β - Bi_2O_3 as a function of pressure up to 27 GPa. For the sake of clarity, a low-frequency region (below 250 cm^{-1}) and a high-frequency region (above 250 cm^{-1}) are plotted in **Figs. 9(a)** and **9(b)**, respectively. **Figures 9(a)** and **(b)** can be divided into four pressure regions: i) from 1 atm to 2 GPa, region of stability of the β phase; ii) from 2 to 15 GPa, region of stability of the β' phase; iii) from 15 GPa to 22 GPa, region where some

peaks of the β' phase start to disappear and new peaks appear, thus indicating the beginning of a phase transition to the χ phase; and iv) above 22 GPa, only the peaks of the χ phase are observed together with signatures of pressure-induced amorphisation likely due to sample decomposition.

In the first region from 1 atm to 2 GPa of **Fig. 9(a)** and **9(b)**, the pressure dependence of fourteen Raman-active modes of β - Bi_2O_3 observed at ambient pressure and two new peaks that appears with pressure increase. **Table III** summarizes the zero-pressure experimental and theoretical frequencies and their pressure coefficients for the Raman-active modes as well as their symmetries. Results previously reported at 1 atm on powder samples [52] are also shown in **Table III** for comparison. Most of these Raman modes can be followed in the second region from 2 to 15 GPa since those modes correspond also to Raman-active modes in β' - Bi_2O_3 . At 2 GPa there are considerable changes in the pressure coefficients of some Raman-active modes. The most notable is the change of the pressure coefficient of the A_1 mode initially at 465 cm^{-1} . This soft mode exhibits a negative pressure coefficient ($-7.6 \text{ cm}^{-1}/\text{GPa}$) up to 2 GPa and, above this pressure, the pressure coefficient is positive ($2.8 \text{ cm}^{-1}/\text{GPa}$). All these changes reinforce the evidence for the pressure-induced IPT taking place near 2 GPa in β - Bi_2O_3 . For this reason, the pressure coefficients of all Raman active modes were calculated in two pressure ranges: below 2 GPa (β phase) and above 2 GPa (β' phase). The good agreement between our experimental and theoretical frequencies and pressure coefficients (see **Fig. 9** and **Table III**) has allowed us to make a tentative assignment of the symmetry of the observed Raman peaks. It must be stressed that the symmetry assignment to experimental Raman peaks is not easy because many peaks overlap due to the large number of Raman modes, as indeed evidenced by our theoretical calculations.

Concerning the pressure dependence of the Raman-active modes of β - Bi_2O_3 , our calculations predict the presence of several soft modes and that some of them undergo anticrossings between 1 and 2 GPa (see **Fig. 9**). The presence of a number of pressure-induced phonon anticrossings at Γ has been recently reported in α - Bi_2O_3 [34]. The most striking feature of the Raman-active modes of β - Bi_2O_3 is the presence of an optic soft A_1 mode near 50 cm^{-1} at 1 atm whose frequency goes to zero near 2 GPa. This soft mode clearly shows a square root pressure dependence before and after 2 GPa; i.e., it can be fitted

to $\omega = A\sqrt{P_T - P}$ below $P_T = 2\text{GPa}$ and to $\omega = B\sqrt{P - P_T}$ above P_T (see **Fig. 10(a)**), where P_T is the transition pressure, and A ($\sim 35\text{ cm}^{-1}\cdot\text{GPa}^{-1/2}$) and B ($\sim 17\text{ cm}^{-1}\cdot\text{GPa}^{-1/2}$) are constants. According to the Landau theory of phase transitions, this soft mode behavior is usually related to a displacive second-order phase transition [76,77]; therefore, it confirms the second-order nature of the pressure-induced IPT in $\beta\text{-Bi}_2\text{O}_3$. Curiously, the square root pressure dependence is also observed in other soft modes of $\beta\text{-Bi}_2\text{O}_3$ (see **Fig. 10(a)**) thus suggesting that the soft low-frequency A_1 mode is coupled to other higher-frequency Raman-active soft modes and that there is more than one soft mode involved in the mechanism of the transformation. This hypothesis is supported by the complex symmetry of the BiO_6 polyhedron in $\beta\text{-Bi}_2\text{O}_3$ and the impossibility to distinguish between low-frequency and high-frequency regions of external and internal modes of the BiO_6 polyhedron since they are very much coupled between them, as in $\alpha\text{-Bi}_2\text{O}_3$ [34].

To further investigate which of the soft modes are indeed related to the mechanism causing the $\beta\text{-}\beta'$ IPT near 2 GPa, we have evaluated the shift of the atoms caused by these vibrational modes and the evolution of the experimental intensities of these modes. From the nine soft modes predicted by our theoretical lattice dynamics calculations, only one was observed experimentally; i.e., the A_1 mode at 465 cm^{-1} . As it can be observed in **Fig. 8** and **Fig. 10(b)**, the intensity of this mode decreases significantly with the increase of pressure up to 2 GPa. Above this pressure, it remains constant despite the low intensity (**Fig. 8**). We think that the decrease in intensity is due to the change in polarizability of the lattice due to the IPT as a consequence of the increase in the symmetry of the BiO_6 polyhedron in the β' phase. Furthermore, the decrease in intensity of the A_1 mode at 465 cm^{-1} with pressure mimics the pressure dependence of the Bi^{3+} eccentricity thus giving support to the existence of the pressure-induced IPT near 2 GPa. A systematic analysis of the eigenvectors of the nine soft modes indicates that all of them contribute partially to the atomic displacements of Bi, O1 and O2 characteristic of the β to β' IPT and shown in **Fig. 6**. In particular, the A_1 mode whose frequency falls to zero at 2 GPa is related to a significant displacement of the Bi and the O1 atoms in the x and z direction, respectively, agreeing with the results plotted in **Fig. 6**. On the other hand, the A_1 mode initially at 453 cm^{-1} and observed experimentally has a strong displacement of the O1 atom in the y and z direction also in good agreement with results plotted in **Fig. 6**. In summary, we propose that the IPT observed at 2 GPa is a

second-order phase transition related to a displacive movement of the atoms in which all the nine soft modes show a partial contribution.

5. Conclusions

Our joint high-pressure experimental and theoretical study of the structural and vibrational properties of synthetic β - Bi_2O_3 at room temperature shows evidence that this compound undergoes a second-order isostructural phase transition (β to β') near 2 GPa. The experimental and theoretical equations of state of the two structures (β and β') as well as the pressure dependence of their Raman-active modes have been reported. Our theoretical lattice dynamics calculations suggest that the isostructural transition is of second-order type and it is driven by nine soft optical vibrational modes that displace the atoms in the β' phase to a more stable and regular position than in the β phase.

In the β' phase the Bi^{3+} environment becomes more regular than in the β phase in good agreement with the decrease of the lone electron pair activity of Bi^{3+} with increasing pressure as indicated by the Bi eccentricity. Interestingly, our results indicate that the isostructural phase transition is not consequence of the vanishing of the lone electron pair activity and care must be taken when eccentricity values obtained at low pressures are extrapolated to high pressures. The extrapolation of the pressure dependence of the eccentricity below 2 GPa at higher pressures could lead to think that the electron pair activity vanishes at 10 GPa; however, our calculation of the eccentricity values in the β' phase above 2 GPa allows us to predict that the vanishing of the lone electron pair activity does not occur at least up to 90 GPa.

Our X-ray diffraction and Raman scattering measurements indicate a partial amorphisation of the structure above 20 and 21.9 GPa, respectively. However, Raman scattering measurements present some weak peaks above 15 GPa, probably related to a new unknown phase which remains up to 27 GPa. On decreasing pressure from 27 GPa, both measurements provide evidence of the decomposition of the sample below 2 GPa which is stimulated by local laser heating.

Acknowledgements

Financial support from the Spanish Consolider Ingenio 2010 Program (MALTA Project No. CSD2007-00045) is acknowledged. This work was also supported by Brazilian Conselho Nacional de Desenvolvimento Científico e Tecnológico (CNPq) under project 201050/2012-9, Spanish MICINN under projects MAT2010-21270-C04-01/03/04 and MAT2013-46649-C4-2/3/4-P, Spanish MINECO under project CTQ2012-36253-C03-02, and from Vicerrectorado de Investigación de la Universitat Politècnica de València under projects UPV2011-0914 PAID-05-11 and UPV2011-0966 PAID-06-11. Supercomputer time has been provided by the Red Española de Supercomputación (RES) and the MALTA cluster. J. A. S. acknowledges Juan de la Cierva fellowship program for his financial support.

References

1. Ai, Z.; Huang, Y.; Lee, S.; Zhang, L. Monoclinic α - Bi_2O_3 Photocatalyst for Efficient Removal of Gaseous NO and HCHO under Visible Light Irradiation. *J. Alloys and Comp.* 2011, 509, 2044-2049.
2. Bessekhoud, Y.; Robert, D.; Weber, J. V. Photocatalytic Activity of $\text{Cu}_2\text{O}/\text{TiO}_2$, $\text{Bi}_2\text{O}_3/\text{TiO}_2$ and $\text{ZnMn}_2\text{O}_4/\text{TiO}_2$ Heterojunctions. *Catal. Today* 2005, 101, 315-321.
3. Cabot, A.; Marsal, A.; Arbiol, J.; Morante, J. R. Bi_2O_3 as a Selective Sensing Material for NO Detection. *Sensors and Actuators B* 2004, 99, 74-89.
4. Zhou, L.; Wang, W. Z.; Xu, H. L.; Sun, S. M.; Shang, M. Bi_2O_3 Hierarchical Nanostructures: Controllable Synthesis, Growth Mechanism, and their Application in Photocatalysis. *Chem. Eur. J.* 2009, 15, 1776-1782.
5. Zheng, F. L.; Li, G. R.; Ou, Y. N.; Wang, Z. L.; Su, C. Y.; Tong, Y. X. Synthesis of Hierarchical Rippled Bi_2O_3 Nanobelts for Supercapacitor Applications. *Chem. Commun.* 2010, 46, 5021-5023.
6. Liu, Y. D.; Xin, F.; Wang, F. M.; Luo, S. X.; Yin, X. H. Synthesis, Characterization, and Activities of Visible Light-Driven Bi_2O_3 - TiO_2 Composite Photocatalysts. *J. Alloys Compd.* 2010, 498, 179-184.
7. Bhande, S. S.; Mane, R. S.; Ghule, A. V.; Han, S. H. A Bismuth Oxide Nanoplate-Based Carbon Dioxide Gas Sensor. *Scripta Mat.* 2011, 65, 1081-1084.
8. Orera, A.; Slater P. R. New Chemical Systems for Solid Oxide Fuel Cells. *Chem. Mat.* 2010, 22, 675-690.
9. Shuk, P.; Wiemhofer, H. D.; Guth, U.; Gopel, W.; Greenblatt, M. Oxide Ion Conducting Solid Electrolytes Based on Bi_2O_3 . *Solid State Ionics* 1996, 89, 179-196.
10. Kharton, V. V.; Marques, F. M. B.; Atkinson, A. Transport Properties of Solid Oxide Electrolyte Ceramics: A Brief Review. *Sol. State Ion.* 2004, 174, 135-149.
11. Hull, S. Superionics: Crystal Structures and Conduction Processes. *Rep. Prog. Phys.* 2004, 67, 1233-1314.

12. Li, R.; Wang, D.; Ge, L.; He, S.; Chen, H.; Guo, L. Effect of Bi₂O₃ on the Electrochemical Performance of LaBaCo₂O_{5+δ} Cathode for Intermediate-Temperature Solid Oxide Fuel Cells. *Ceramics Int.* 2014, 40, 2599-2603.
13. Elbatal, F. H. Gamma Ray Interaction with Bismuth Silicate Glasses. *Nucl. Instr. and Meth. in Phys. Res. B* 2007, 254, 243-253.
14. Bajaj, A.; Khanna, A.; Chen, B. G.; Longstaffe, J. G.; Zwanziger, U. -W.; Zwanziger, J. W.; Gómez, Y.; González, F. Structural Investigation of Bismuth Borate Glasses and Crystalline Phases. *J. Non-Cryst. Solids* 2009, 355, 45-53.
15. Chanthima, N.; Kaewkhao, J.; Kedkaew, C.; Chewpraditkul, W.; Pokaipist, A.; Limsuwan, P. Study on Interaction of Bi₂O₃, PbO and BaO in Silicate Glass System at 662 keV for Development of Gamma-Rays Shielding Materials. *Prog. Nucl. Sci. Tech.* 2011, 1, 106-109.
16. Won-in, K.; Pongkrapan, S.; Dararutana, P. Eco-Glass Based on Thailand Quartz Sands and Bismuth Oxide. *Mat. Sci. Forum* 2011, 695, 223-226.
17. Maeder, T. Review of Bi₂O₃ Based Glasses for Electronics and Related Applications. *Int. Mat. Rev.* 2013, 58, 3-40.
18. Iyyapushpam, S.; Nishanthi, S. T.; Padiyan, D. P. Synthesis of Room Temperature Bismuth Oxide and Its Photocatalytic Activity. *Mat. Lett.* 2012, 86, 25-27.
19. Cheng, L.; Kang, Y. Selective Preparation of Bi₂O₃ Visible Light-Driven Photocatalyst by Dispersant and Calcinations. *J. Alloys Comp.* 2014, 585, 85-93.
20. Matsumoto, A.; Koyama, Y.; Tanaka, I. Structures and Energetics of Bi₂O₃ Polymorphs in a Defective Fluorite Family Derived by Systematic First-Principle Lattice Dynamics Calculation. *Phys. Rev. B* 2010, 81, 094117.
21. Matsumoto, A.; Koyama, Y.; Togo, A.; Choi, M.; Tanaka, I. Electronic Structures Of Dynamically Stable As₂O₃, Sb₂O₃, and Bi₂O₃ Crystal Polymorphs. *Phys. Rev. B* 2011, 83, 214110.
22. Harwig, H. A. On the Structure of Bismuthsesquioxide: α , β , γ and δ -Phase. *Z. Anorg. and Allg. Chem.* 1978, 444, 151-166.
23. Sammes, N. M.; Tompsett, G. A.; Nafe, H.; Aldinger, F. Bismuth Based Oxide Electrolytes - Structure and Ionic Conductivity. *J. Eur. Cer. Soc.* 1999, 19, 1801-1826.
24. Salazar-Pérez, A. J.; Camacho-López, M. A.; Morales-Luckie, R. A.; Sánchez-Mendieta, V.; Ureña-Núñez, F.; Arenas-Alatorre, J. Structural Evolution of Bi₂O₃ Prepared by Thermal Oxidation of Bismuth Nano-Particles. *Superf. Vac.* 2005, 18(3), 4-8.
25. Nunn, S. D.; Payzant, E. A. Properties of Ionic-Conducting β -Bi₂O₃ Containing Mixed Dopants. *J. Am. Ceram. Soc.* 2002, 85, 2633-2636.
26. Gomez, C. L.; Depablos-Rivera, O.; Medina, J. C.; Silva-Bermudez, P.; Muhl, S.; Zeinert, A.; Rodil, S. E. Stabilization of the Delta-Phase in Bi₂O₃ Thin Films. *Sol. State Ion.* 2014, 225, 147-152.
27. Yan, Y.; Zhou, Z.; Cheng, Y.; Qiu, L.; Gao, C.; Zhou, J. Template-Free Fabrication of α - and β - Bi₂O₃ Hollow Spheres and Their Visible Light Photocatalytic Activity for Water Purification. *J. Allo. Comp.* 2014, 605, 102-108.
28. Gualtieri, A. F.; Immovilli, S.; Prudenziati, M. Powder X-ray Diffraction Data for the New Polymorphic Compound ω -Bi₂O₃. *Pow. Diffraction.* 1997, 12, 90-92.
29. Kumada, N.; Kinomura, N. A New Allotropic Form of Bi₂O₃. *Mat. Res. Soc. Symp. Proc.* 1999, 547, 227-232.

30. Ghedia, S.; Locherer, T.; Dinnebier, R.; Prasad, D. L. V. K.; Wedig, U.; Jansen, M.; Senyshyn, A. High-Pressure and High-Temperature Multianvil Synthesis of Metastable Polymorphs of Bi₂O₃: Crystal Structure and Electronic Properties. *Phys. Rev. B* 2010, 82, 024106.
31. Locherer, T.; Dasari, L.; Prasad, V. K.; Dinnebier, R.; Wedig, U.; Jansen, M.; Garbarino, G.; Hansen, T. High-Pressure Structural Evolution of HP-Bi₂O₃. *Phys. Rev. B* 2011, 83, 214102.
32. Chouinard, C.; Desgreniers, S. Bi₂O₃ under Hydrostatic Pressure: Observation of a Pressure-Induced Amorphisation. *Solid State Communication* 2000, 113, 125-129.
33. Pereira, A. L. J.; Errandonea, D.; Beltrán, A.; Gracia, L.; Gomis, O.; Sans, J. A.; García-Domene, B.; Miquel-Veyrat, A.; Manjón, F. J.; Muñoz, A.; Popescu, C. Structural Study of α -Bi₂O₃ under Pressure. *J. Phys.: Condens. Matter* 2013, 25, 475402.
34. Pereira, A. L. J.; Gomis, O.; Sans, J. A.; Pellicer-Porres, J.; Manjon, F. J.; Betran, A.; Rodriguez-Hernandez, P.; Muñoz, A. Pressure Effects on the Vibrational Properties of α -Bi₂O₃: An Experimental and Theoretical Study. *J. Phys. Cond. Matter* 2014, 26, 225401.
35. Cheng, H.; Huang, B.; Lu, J.; Wang, Z.; Xu, B.; Qin, X.; Zhang, X.; Dai Y. Synergistic Effect of Crystal and Electronic Structures on the Visible-Light-Driven Photocatalytic Performances of Bi₂O₃ Polymorphs. *Phys. Chem. Chem. Phys.* 2010, 12, 15468-15475.
36. Brezesinski, K.; Ostermann, R.; Hartmann, P.; Perlich, J.; Brezesinski, T. Exceptional Photocatalytic Activity of Ordered Mesoporous β -Bi₂O₃ Thin Films and Electrospun Nanofiber Mats. *Chem. Mater.* 2010, 22, 3079-3085.
37. Li, M.; Li, F.; Yin, P. G. Tailoring the Band Structure of β -Bi₂O₃ by co-Doping for Realized Photocatalytic Hydrogen Generation. *Chem. Phys. Lett.* 2014, 601, 92-97.
38. Fauth, F.; Peral, I.; Popescu, C.; Knapp, M. The New Material Science Powder Diffraction Beamline at ALBA Synchrotron. *Powd. Diffract.* 2013, 28, S360-S370.
39. Mao, M. K.; Xu, J.; Bell P. M. Calibration of the Ruby Pressure Gauge to 800-Kbar under Quasi-Hydrostatic Conditions. *J. Geophys. Res.* 1986, 91, 4673-4676.
40. Hammersley, A. P.; Svensson, S. O.; Hanfland, M.; Fitch, A. N.; Häusermann, D. Two-Dimensional Detector Software: From Real Detector to Idealized Image or Two-Theta Scan. *High Pressure Research* 1996, 14, 235-248.
41. Kraus, W.; Nolze, G. POWDER CELL - A Program for the Representation and Manipulation of Crystal Structures and Calculation of the Resulting X-Ray Powder Patterns. *J. Appl. Crystallogr.* 1996, 29, 301-303.
42. Larson, A. C.; von Dreele, R. B. LANL Report 2004, 86-748.
43. Toby, B. H. EXPGUI, A Graphical User Interface for GSAS. *J. Appl. Cryst.* 2001, 34, 210-213.
44. Balic-Zunic, T.; Vickovic, I. IVTON - Program for the Calculation of Geometrical Aspects of Crystal Structures and Some Crystal Chemical Applications. *J. Appl. Crystallogr.* 1996, 29, 305-306.
45. Debernardi, A.; Urlich, C.; Cardona, M.; Syassen, K. Pressure Dependence of Raman Linewidth in Semiconductors. *Phys. Stat. Sol. B* 2001, 223, 213-223.
46. Hohenberg, P.; Kohn, W. Inhomogeneous Electron Gas. *Phys. Rev. B* 1964, 136, 3864.
47. Blöchl, P. E. Projector augmented-wave method. *Phys. Rev. B* 1994, 50, 17953-17979.

48. Perdew, J. P.; Ruzsinszky, A.; Csonka, G. I.; Vydrov, O. A.; Suseria, G. E.; Constantin, L. A.; Zhou, X.; Burke, K. Restoring the Density-Gradient Expansion for Exchange in Solids and Surfaces. *Phys. Rev. Lett.* 2008, 100, 136406.
49. Parlinski, K.; Li, Z. Q.; Kawazoe, Y. First-Principles Determination of the Soft Mode in Cubic ZrO₂. *Phys. Rev. Lett.* 1997, 78, 4063-4066.
50. Efthimiopoulos, I.; Kemichick, J.; Zhou, X.; Khare, S. V.; Ikuta, D.; Wang, Y. High-Pressure Studies of Bi₂S₃. *J. Phys. Chem. A* 2014, 118, 1713-1720.
51. Blower, S. K.; Greaves, C. The Structure of β -Bi₂O₃ from Powder Neutron Diffraction Data. *Acta Cryst.* 1988, 44, 587-589.
52. Salazar-Pérez, A. J.; Camacho-López, M. A.; Morales-Luckie, R. A.; Sánchez-Mendieta, V.; Ureña-Núñez, F.; Arenas-Alatorre, J. Structural Evolution of Bi₂O₃ Prepared By Thermal Oxidation of Bismuth Nano-Particles. *Superf. y Vac.* 2005, 18(3), 4-8.
53. Monnereau, O.; Tortet, L.; Llewellyn, P.; Rouquerol, F.; Vacquier, G. Synthesis of Bi₂O₃ by Controlled Transformation Rate Thermal Analysis: A New Route for This Oxide? *Solid State Ionics* 2003, 157, 163-169.
54. Chen, R.; Shen, Z.-R.; Wang, H.; Zhou, H.-J.; Liu, Y.-P.; Ding, D.-T.; Chen, T.-H. Fabrication of Mesh-Like Bismuth Oxide Single Crystalline Nanoflakes and Their Visible Light Photocatalytic Activity. *J. Alloys Compd.* 2011, 509, 2588-2596.
55. Qiu, Y.; Yang, M.; Fan, H.; Zuo, Y.; Shao, Y.; Xu, Y.; Yang, X.; Yang, S. Nanowires of α - and β -Bi₂O₃: Phase-Selective Synthesis and Application in Photocatalysis. *Cryst. Eng. Comm* 2011, 13, 1843-1850.
56. Ayala, A.; López-García, A.; Leyva A. G.; de Benyacar, M. A. R. Stabilization of β -Bi₂O₃ by Hafnia. *Solid State Commun.* 1996, 99, 451-455.
57. Jovalekic, C.; Zdujic, M.; Poleti, D.; Karanovic, L.; Mitric, M. Structural and Electrical Properties of the 2Bi₂O₃ · 3ZrO₂ System. *J. Sol. State Chem.* 2008, 181, 1321-1329.
58. Akahama, Y.; Kawamura, H.; Singh, A. K. Equation of states of Bismuth to 222 GPa and Comparison of Gold and Platinum Pressure Scales to 145 GPa. *J. Appl. Phys* 2002, 92, 5892-5897.
59. Frogley, M. D.; Sly, J. L.; Dunstan, D. J. Pressure Dependence of the Direct Band Gap in Tetrahedral Semiconductors. *Phys. Rev. B* 1998, 58, 12579-12582.
60. Pereira, A. L. J.; Gracia, L.; Santamaría-Pérez, D.; Vilaplana, R.; Manjón, F. J.; Errandonea, D.; Nalin, M.; Beltrán, A. Structural and Vibrational Study of Cubic Sb₂O₃ under High Pressure. *Phys. Rev. B* 2012, 85, 174108.
61. Schneider, V. E.; Tornau, E. E. On the Theory of Isostructural Phase Transition in Crystals. *Phys. Stat. Sol. B* 1982, 111, 565-574.
62. Pandey, K. K.; Poswal, H. K.; Kumar, R.; Sharma, S. M. High Pressure Iso-Structural Phase Transition in BiMn₂O₅. *J. Phys. Condes. Matter.* 2013, 32, 325401.
63. Friedrich, A.; Juarez-Arellano, E. A.; Haussuhl, E.; Boehler, R.; Winkler, B.; Wiehl, L.; Morgenroth, W.; Burianek, M.; Muhlberg, M. Persistence of the Stereochemical Activity of the Bi³⁺ Lone Electron Pair in Bi₂Ga₄O₉ up to 50 GPa and Crystal Structure of the High-Pressure Phase. *Acta Cryst. B* 2010, 66, 323-337.
64. Zunic, T. B.; Makovicky, E. Determination of the Centroid or 'The Best Centre' of a Coordination Polyhedron. *Acta Cryst. B* 1996, 52, 78-81.

65. Olsen, L.A.; López-Solano, J.; García, A.; Balic-Zunic, T.; Makovicky, E. Dependence of the Lone Pair of Bismuth on Coordination Environment and Pressure: An *ab Initio* Study on $\text{Cu}_4\text{Bi}_5\text{S}_{10}$ and Bi_2S_3 . *J. Solid State Chem.* 2010, 183, 2133-2143.
66. Lundegaard, L. F.; Makovicky, E.; Boffa-Ballaran, T.; Zunic, T. B. Crystal Structure and Cation Lone Electron Pair Activity of Bi_2S_3 between 0 and 10 GPa. *Phys. Chem. Miner* 2005, 32, 578-584.
67. Olsen, L. A.; Zunic, T. B.; Makovicky, E.; Ullrich, A.; Miletich, R. Hydrostatic Compression of Galenobismutite (PbBi_2S_4): Elastic Properties and High-Pressure Crystal Chemistry. *Phys. Chem. Miner.* 2007, 34, 467-475.
68. Olsen, L. A.; Zunic, T. B.; Makovicky, E. High-Pressure Anisotropic Distortion of $\text{Pb}_3\text{Bi}_2\text{S}_6$: a Pressure-Induced, Reversible Phase Transition with Migration of Chemical Bonds. *Inorg. Chem.* 2008, 47, 6756-6762.
69. Olsen, L. A.; Friese, K.; Makovicky, E.; Balic-Zunic, T.; Morgenroth, W.; Grzechnik, A. Pressure Induced Phase Transition in $\text{Pb}_6\text{Bi}_2\text{S}_9$. *Phys. Chem. Minerals* 2011, 38, 1-10.
70. Friedrich, A.; Biehler, J.; Morgenroth, W.; Wiehl, L.; Winkler, B.; Hanfland, M.; Tolkiehn, M.; Burianek, M.; Mühlberg, M. High-Pressure Phase Transition of $\text{Bi}_2\text{Fe}_4\text{O}_9$. *J. Phys.: Condens. Matter* 2012, 24, 145401.
71. Stoltzfus, M. W.; Woodward, P. M.; Seshadri, R.; Klepeis, J. -H.; Bursten, B. Structure and Bonding in SnWO_4 , PbWO_4 , and BiVO_4 : Lone Pairs vs Inert Pairs. *Inorg. Chem.* 2007, 46, 3839-3850.
72. Denisov, V. N.; Ivlev, A. N.; Lipin, A. S.; Mavrin, B. N.; Orlov, V. G. Raman Spectra and Lattice Dynamics of Single-Crystal $\alpha\text{-Bi}_2\text{O}_3$. *J. Phys.: Condens. Matter.* 1997, 9, 4967-4978.
73. Olijnyk, H.; Nakano, S.; Takemura, K. First- and Second Order Raman Scattering in Sb and Bi at High Pressure. *Phys. Stat. Sol B* 2007, 10, 3572-3582.
74. Lundegarrd, L. F.; Weck, G.; McMahon, M. I.; Desgreniers, S. Observation of an O_8 Molecular Lattice in the ϵ Phase of Solid Oxygen. *Nature* 2006, 443, 201-204.
75. Weck, G.; Loubeyre, P.; LeToullec, R. Observation of Structural Transition in Metal Oxygen. *Phys. Rev. Lett.* 2002, 88, 035504.
76. Errandonea, D.; Manjón, F. J. On the Ferroelastic Nature of the Scheelite-To-Fergusonite Phase Transition in Orthotungstates and Orthomolybdates. *Mat. Res. Bull.* 2009, 44, 807-811.
77. Dove, M. T. Theory of Displacive Phase Transitions in Minerals. *Am. Miner.* 1997, 82, 213-244.

Tables

Table I - Experimental and theoretical atomic coordinates of synthetic β - Bi_2O_3 at 1 atm and theoretical atomic coordinates of β' - Bi_2O_3 at 2.3 GPa.

Atom	Site		1 atm			2.3 GPa		
			x	y	z	x	y	z
Bi	8e	Theor.	0.0213	0.257	0.231	0.000	0.252	0.221
		Exp.	0.01902(14)	0.25420(26)	0.2378(4)			
O1	8e	Theor.	0.289	0.313	0.034	0.297	0.297	0.000
		Exp.	0.3006(25)	0.3149(23)	0.014(4)			
O2	4d	Theor.	0.000	0.500	0.405	0.000	0.500	0.397
		Exp.	0.000	0.500	0.379(4)			

Table II - EOS parameters and axial compressibility at zero pressure of β -Bi₂O₃.

	V_0 (\AA^3)	B_0 (GPa)	B'_0	κ_a (10^{-3} GPa^{-1})	κ_c (10^{-3} GPa^{-1})
Experimental (all range)	337.1(7)	33(3)	14(2)	10.1(5)	9.7(4)
Theoretical (all range)	332.1(8)	39.7(30)	11.1(9)	10.5(1)	6.34(4)
Experimental (up to 2 GPa)	337.9(3)	38(1)	4.0 (fixed)	13.5(5)	6.2(1)
Theoretical (up to 2GPa)	334.8(2)	32.5(5)	4.0 (fixed)	12.9(6)	7.7(2)
Experimental (from 2 to 12 GPa)	327(2)	77(2)	4.0 (fixed)	4.1(1)	5.8(2)
Theoretical (from 2 to 12 GPa)	322.8(5)	84(1)	4.0 (fixed)	4.88(7)	6.28(6)

Table III – Experimental and theoretical Raman mode frequencies and pressure coefficients of β -Bi₂O₂ obtained by fitting the equation $\omega(P) = \omega_0 + a \cdot P$ compared with those obtained by Pérez-Salazar et al. [52] at ambient conditions. To perform the fit, data were separated in two regions: from 1 atm to 2 GPa (β phase) and from 2 GPa onwards (β' phase).

Symmetry	Experimental			Theoretical			Ref. [52]
	ω_0 (cm ⁻¹)	a (cm ⁻¹ /GPa) 0-2 GPa	a (cm ⁻¹ /GPa) from 2 GPa	ω_0 (cm ⁻¹)	a (cm ⁻¹ /GPa) 0-2 GPa	a (cm ⁻¹ /GPa) from 2 GPa	ω_0 (cm ⁻¹)
	B ₁	30	0.29		27.05	-1.29	1.38
A ₁				48.04	-22.0	2.43	
E	48	2.96	0.53	54.64	2.68	0.30	
E	66	5.45	2.72	63.68	0.42	2.05	69
E		0.23	1.51	71.95	5.03	1.54	
B ₁				80.26	-0.98	1.14	
A ₁	89	7.32	0.97	89.20	5.92	0.93	
E	94	6.56	2.71	90.33	6.31	1.11	93
E				102.14	5.02	2.47	
B ₂				118.09	3.90	1.74	
B ₁	124	3.72	0.87	121.06	3.33	0.69	
A ₁	127	4.01	2.23	130.16	4.60	1.94	128
B ₂	142	4.38	4.06	145.57	6.70	2.20	
A ₁				158.98	8.74	1.84	
E	161	2.94		165.15	3.43	1.65	
E				170.26	6.65	2.81	
B ₁				171.33	-1.98	3.32	
B ₂	197*			180.93	0.17	2.60	
E				223.00	0.29	1.21	
E	231	7.22	2.76	240.34	9.42	2.46	
B ₁				265.79	0.18	3.14	
E				273.20	3.04	3.38	
A ₁	313	1.84	1.84	294.98	1.67	2.72	317
B ₂	326	-2.20	1.80	298.92	-0.70	3.60	
A ₁				304.02	6.67	3.71	
B ₂				318.10	-4.65	1.95	
E				340.38	-19.04	4.12	
A ₁	465	-7.61	3.17	452.73	-5.29	3.57	461

E			459.67	8.15	3.22
B ₁			461.41	7.53	4.12
E	497**	3.27	489.46	0.99	3.26
B ₁			530.19	-1.38	2.95
B ₂			532.16	2.01	2.7
E			584.20	5.9	2.8
E			603.34	5.1	2.8

* The peak disappears with pressure increase

**Peak not observed at 1 atm

Figure Captions

Figure 1 – (color online) (a) Crystalline structure of tetragonal β - Bi_2O_3 at 1 atm. (b) The structure of β - Bi_2O_3 is projected along the c -axis in order to allow the observation of the atoms arranged in slightly distorted sheets. Grey balls represent Bi atoms, while red balls represent O atoms. The structure is composed by one Bi with coordination six (light blue polyhedral).

Figure 2 - (color online) Characterization of β - Bi_2O_3 samples at ambient conditions: (a) Powder XRD pattern showing the Rietveld refined spectrum (red dotted line) and residues (blue lower line); (b) RS spectra; (c) SEM image; and (d) EDX analysis.

Figure 3 - (color online) Angle-dispersive XRD of β - Bi_2O_3 measured at different pressures up to 27.2 GPa at room temperature. The top pattern corresponds to the recovered sample at 1.3 GPa after decompression from 27.2 GPa.

Figure 4 - Experimental (symbols) and theoretical (lines) pressure dependence of (a) the lattice parameters a and c and (b) c/a ratio.

Figure 5 - (color online) Unit-cell volume vs. pressure for β - Bi_2O_3 . Symbols represent experimental data and solid line the theoretical data. Red (blue) solid line corresponds to the 3rd-order Birch-Murnaghan EOS fit to experimental data from 0 to 2 GPa (2 to 12 GPa).

Figure 6 - (color online) Experimental (squares) and theoretical (solid lines) evolution of the (a) Bi, (b) O1 and (c) O2 atomic coordinates of the different Wyckoff positions in β - Bi_2O_3 as a function of pressure.

Figure 7 - (color online) (a) Theoretical evolution of the Bi - O bond lengths with pressure. (b) Experimental (black) and theoretical (red) evolution of the Bi eccentricity with pressure.

Figure 8 - (color online) Room-temperature Raman spectra of β - Bi_2O_3 at selected pressures up to 27 GPa. The top patterns correspond to the recovered sample after decompression from 27 GPa.

Figure 9 - (color online) Experimental (symbols) and theoretical (lines) pressure dependence of the Raman-active modes of β - Bi_2O_3 : (a) from 0 to 250 cm^{-1} ; (b) from 230 to 700 cm^{-1} . Different colors represent Raman-active modes of different symmetries.

Figure 10 - (color online) (a) Pressure dependence of the experimental (symbols) and theoretical (lines) square frequency of two A_1 and one E soft modes. (b) Pressure dependence of the experimental absolute intensity of the 465 cm^{-1} peak at 1 atm (calculations locate it at 452 cm^{-1}) and attributed to the high-frequency A_1 mode.

Figure 1

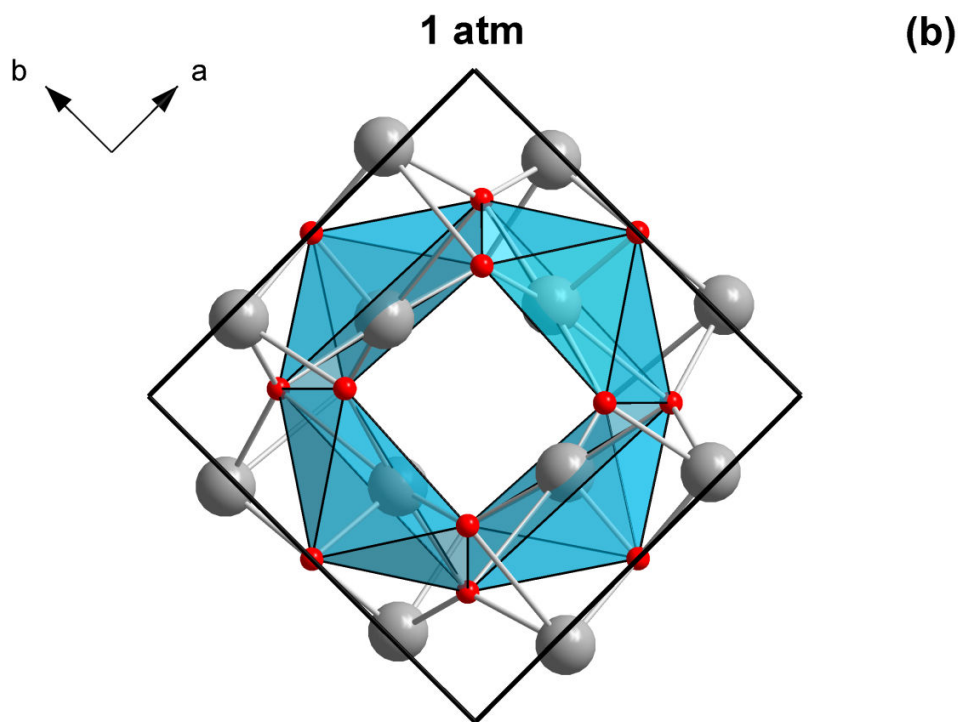
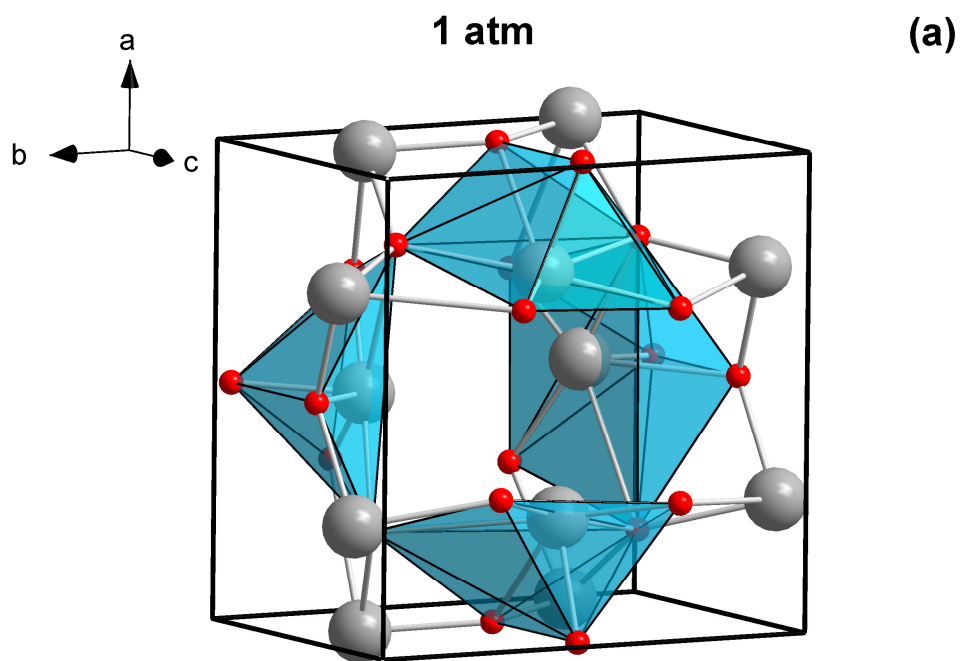


Figure 2

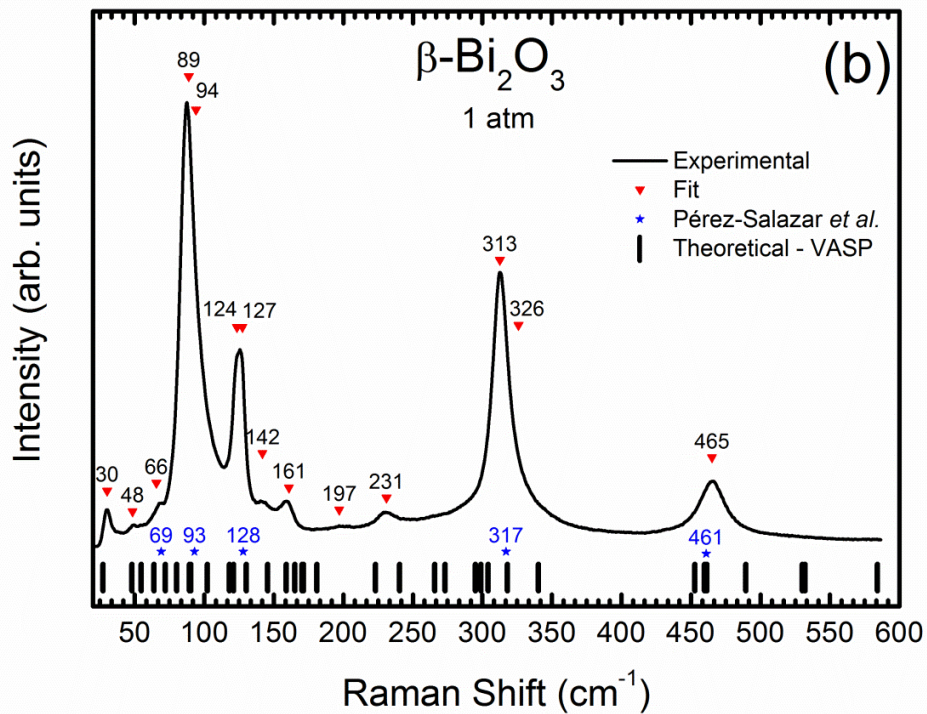
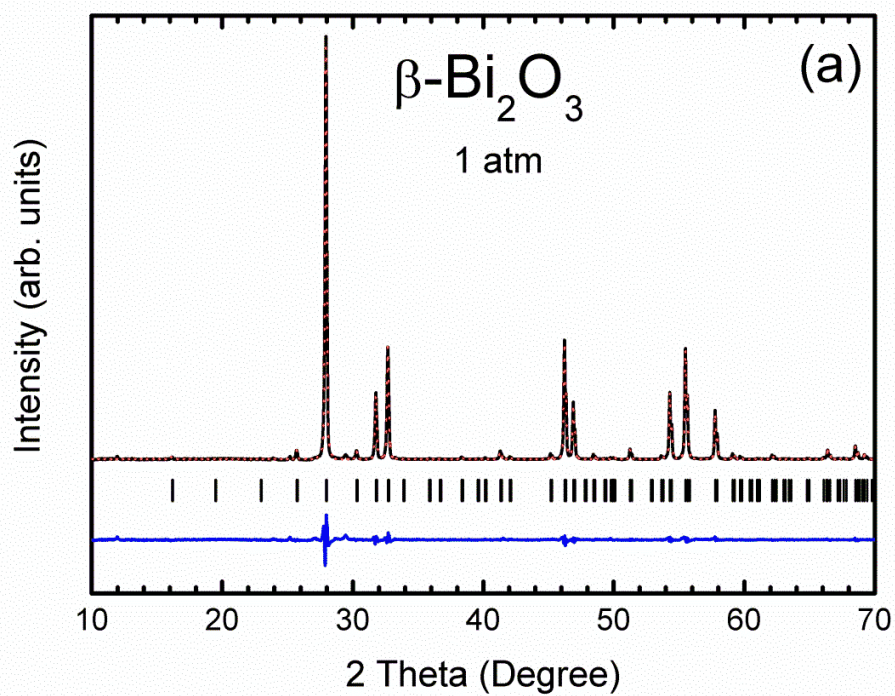


Figure 2

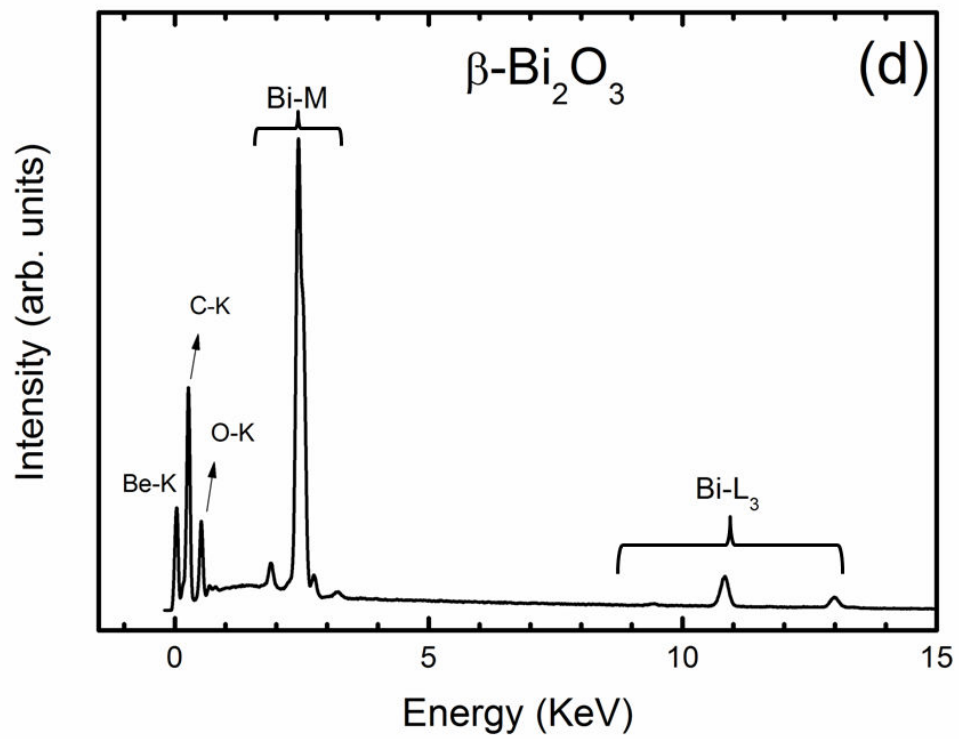
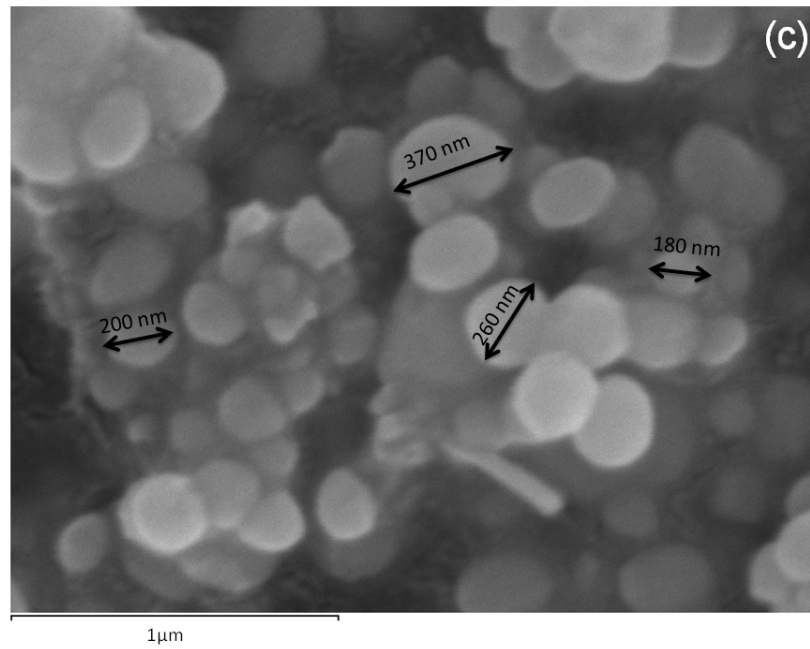


Figure 3

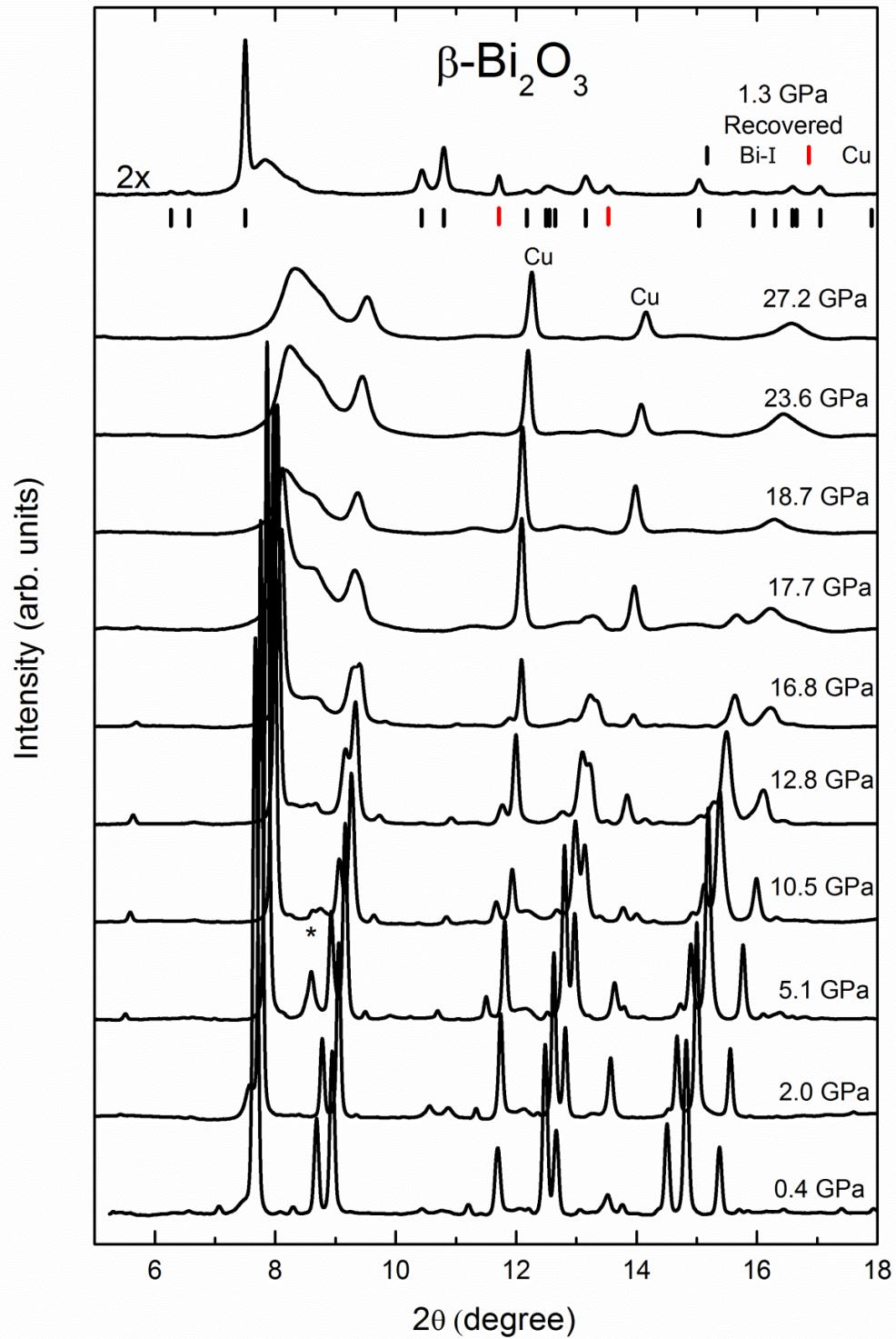


Figure 4

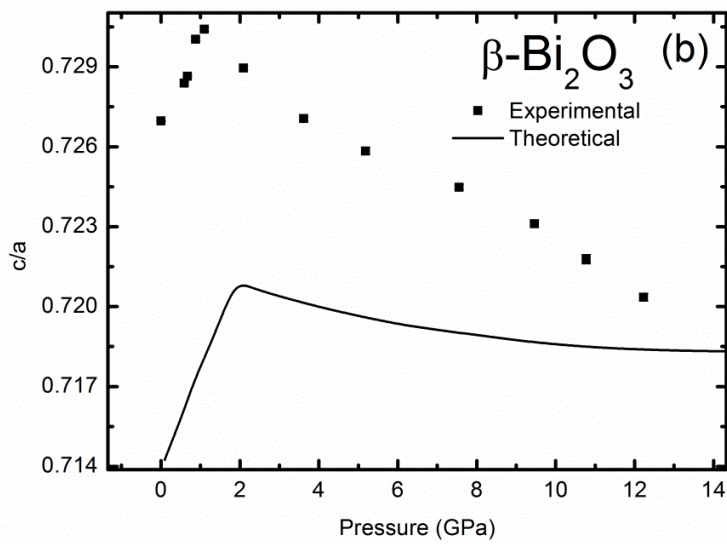
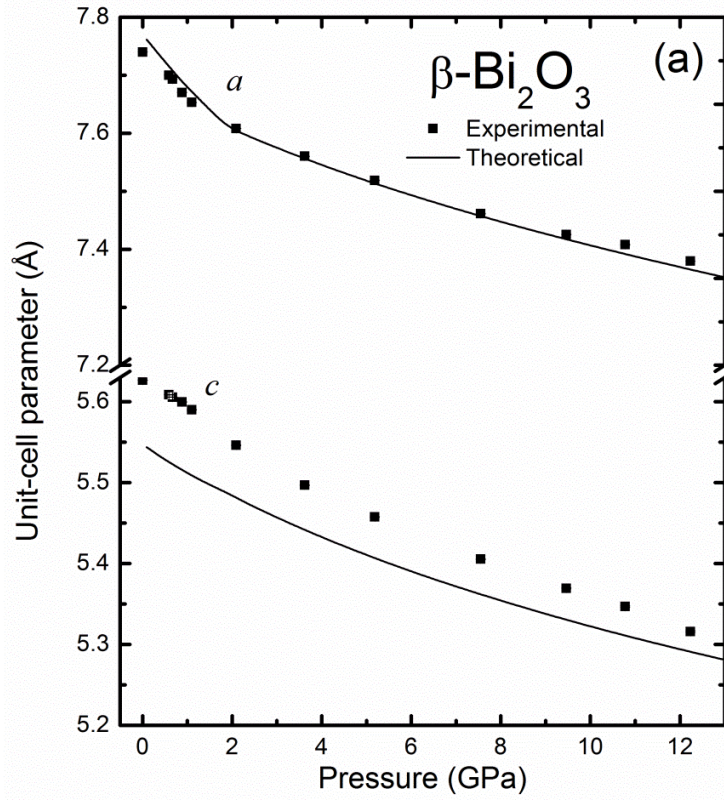


Figure 5

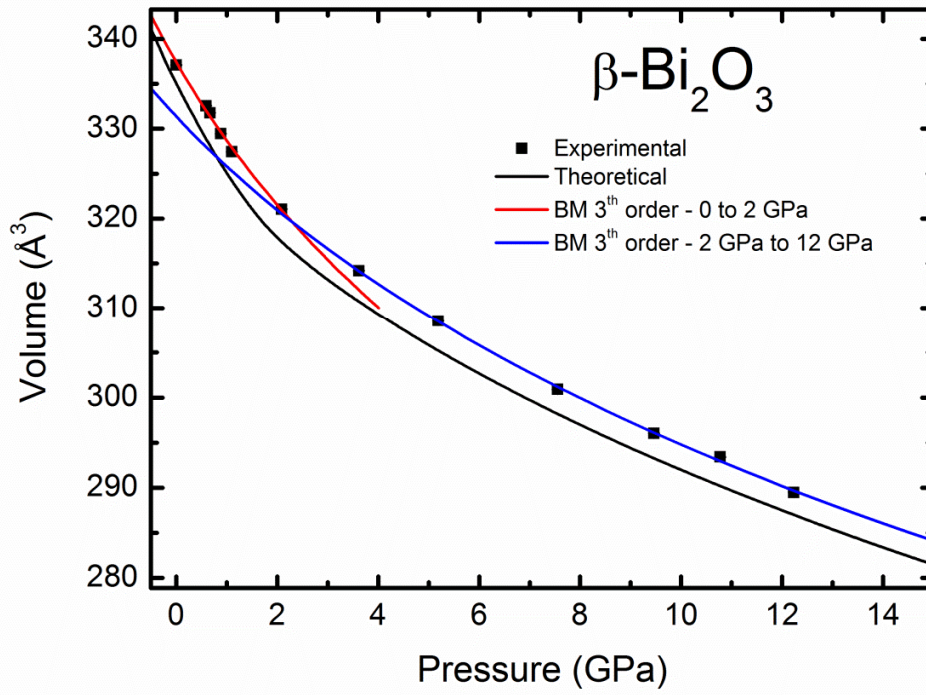


Figure 6

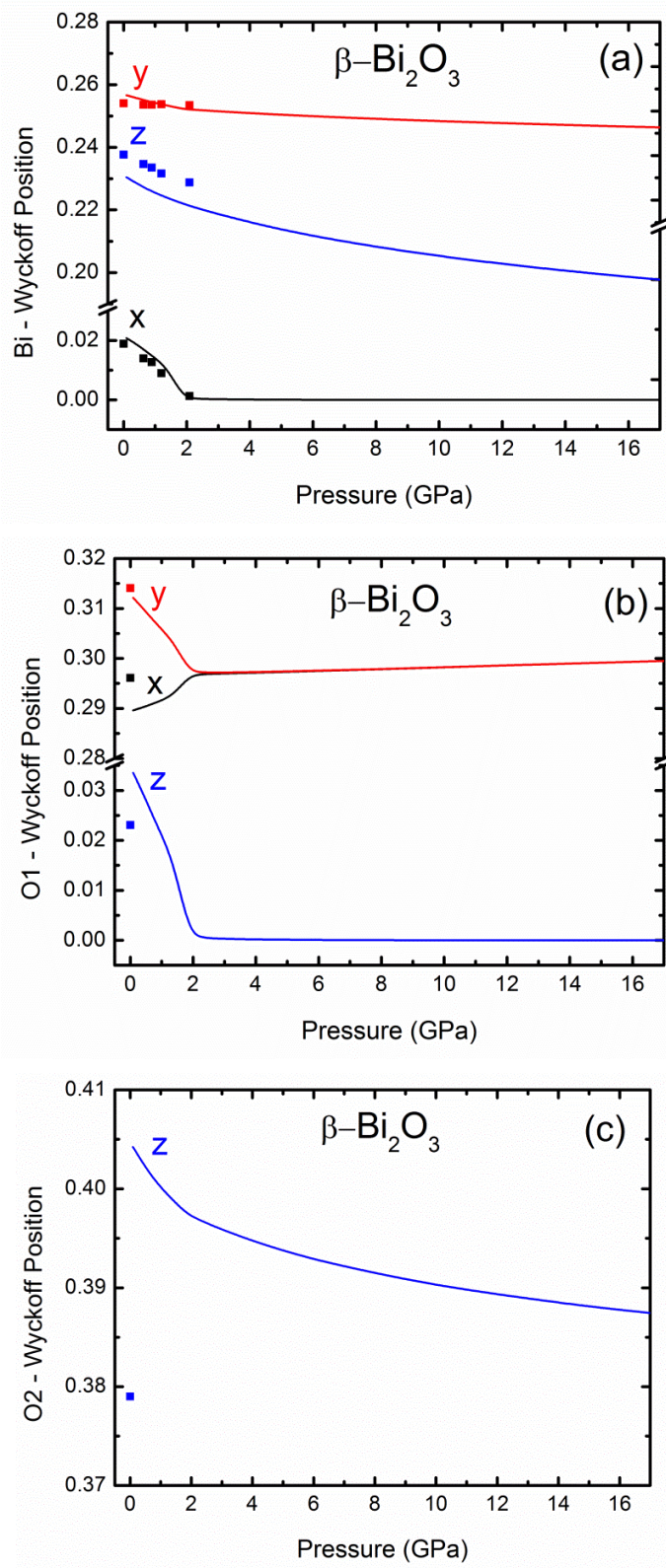


Figure 7

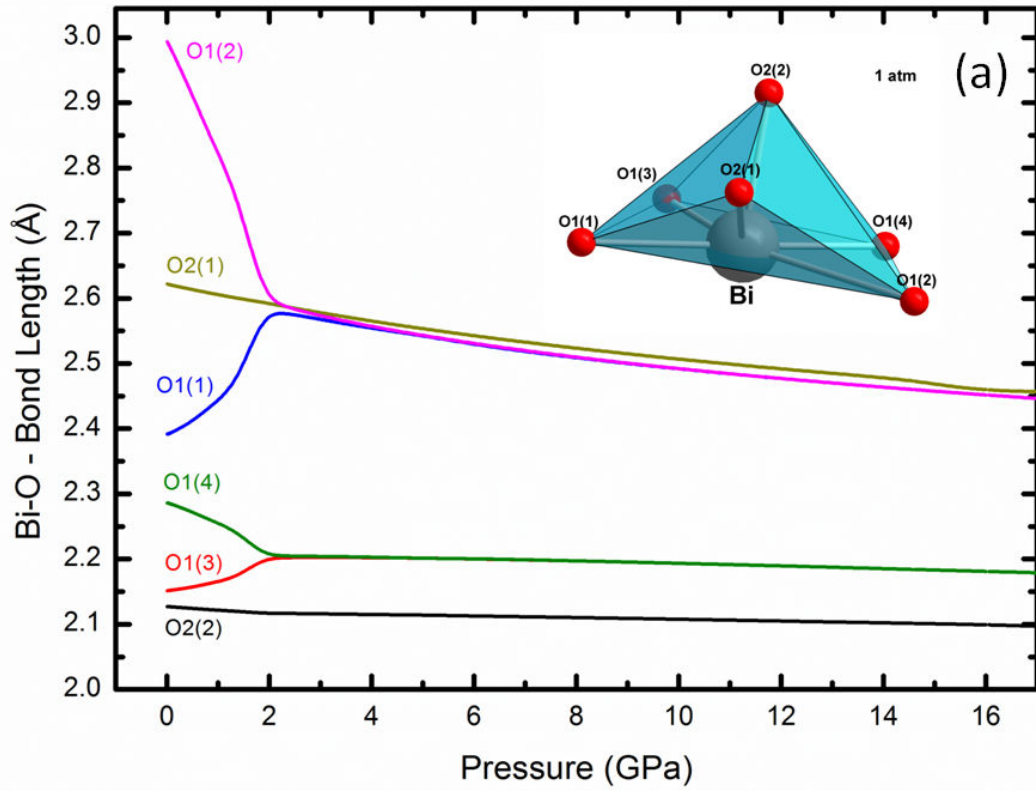


Figure 7

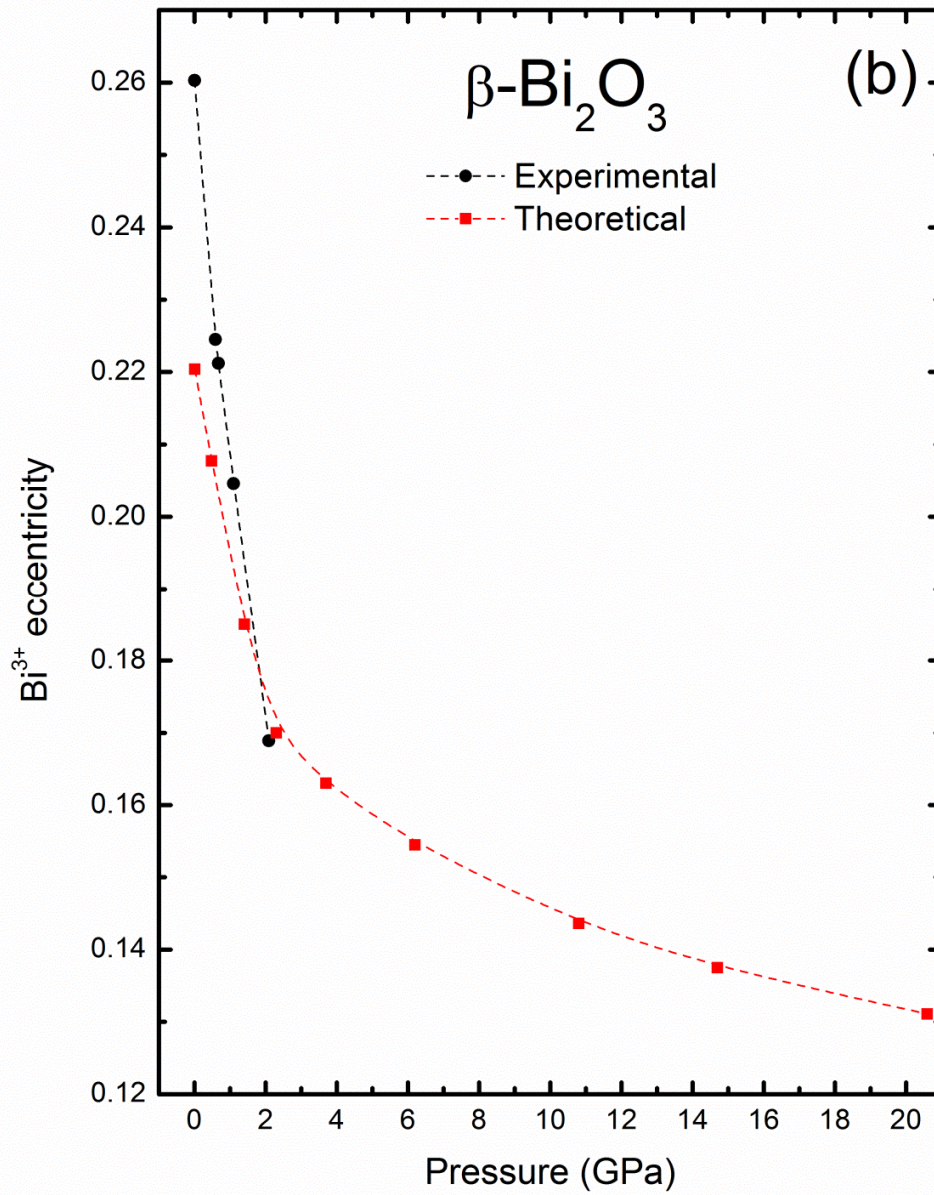


Figure 8

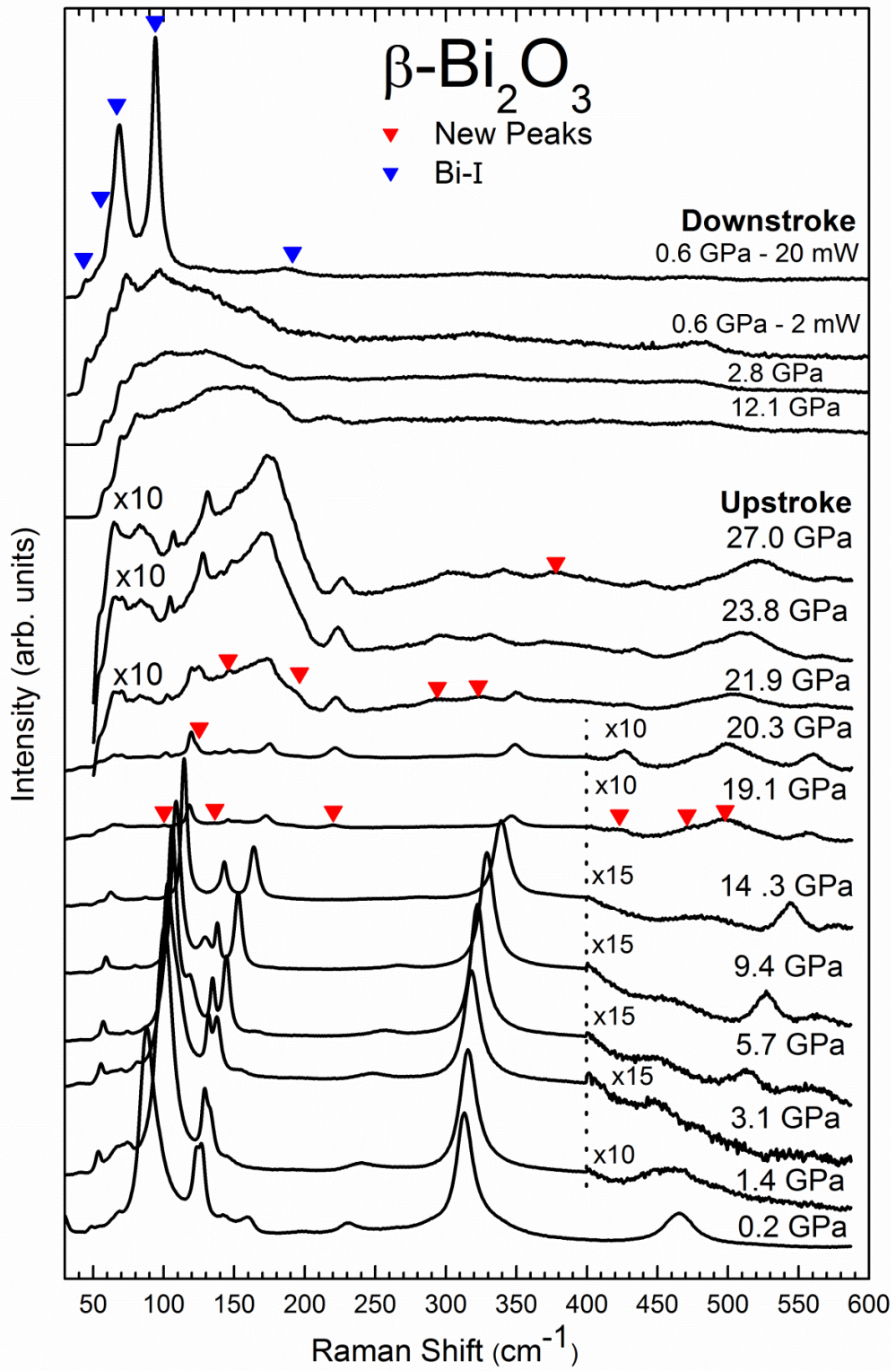


Figure 9

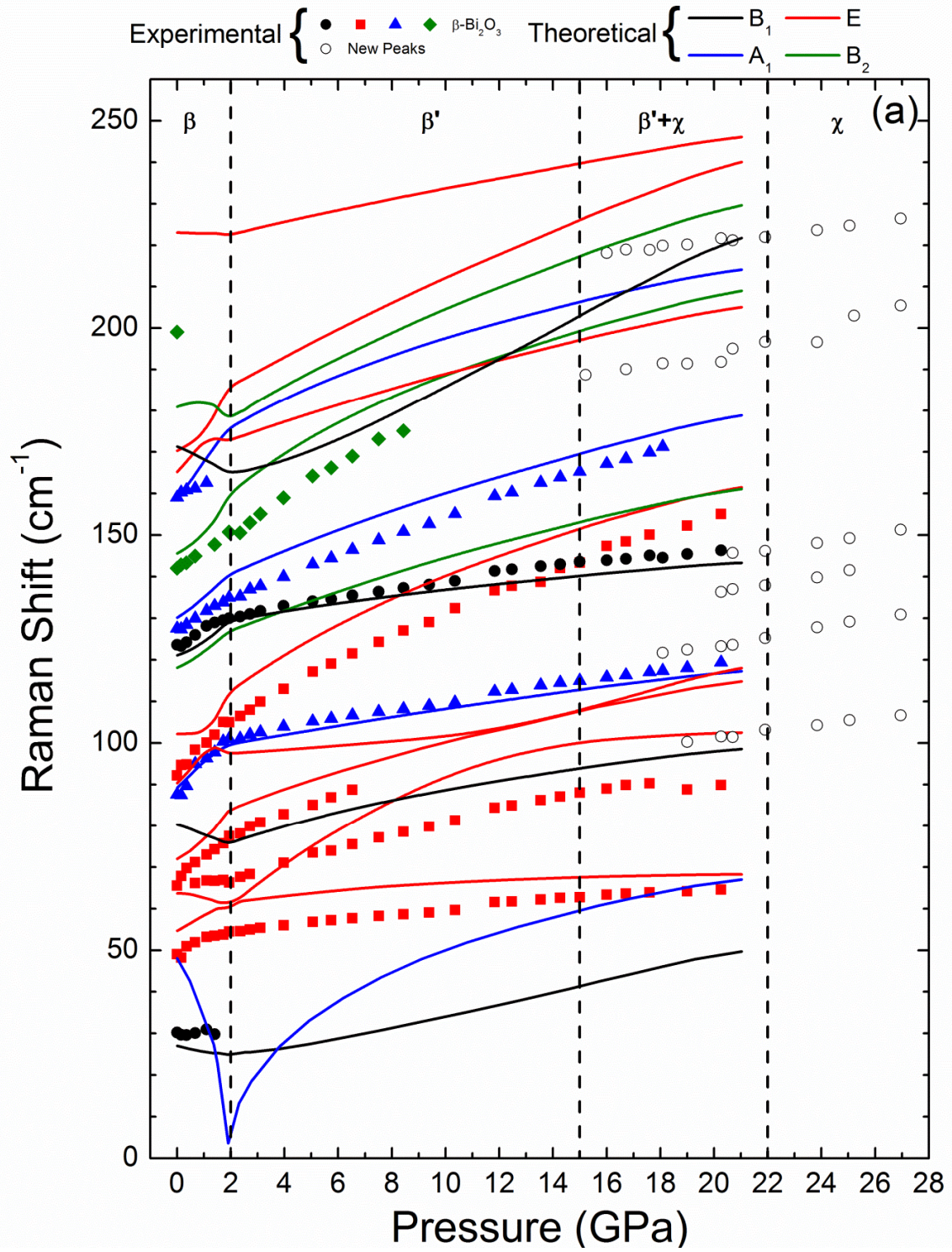


Figure 9

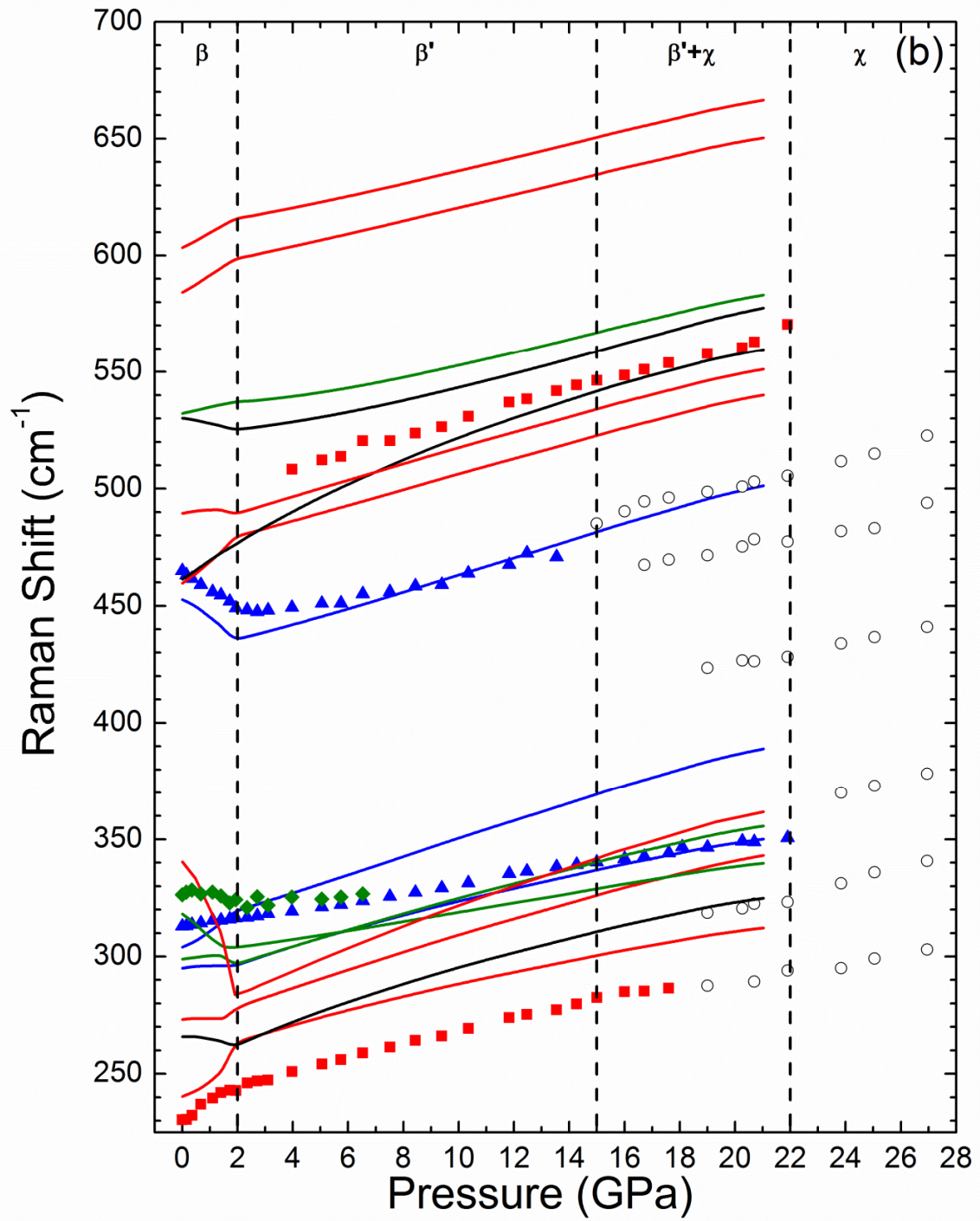


Figure 10

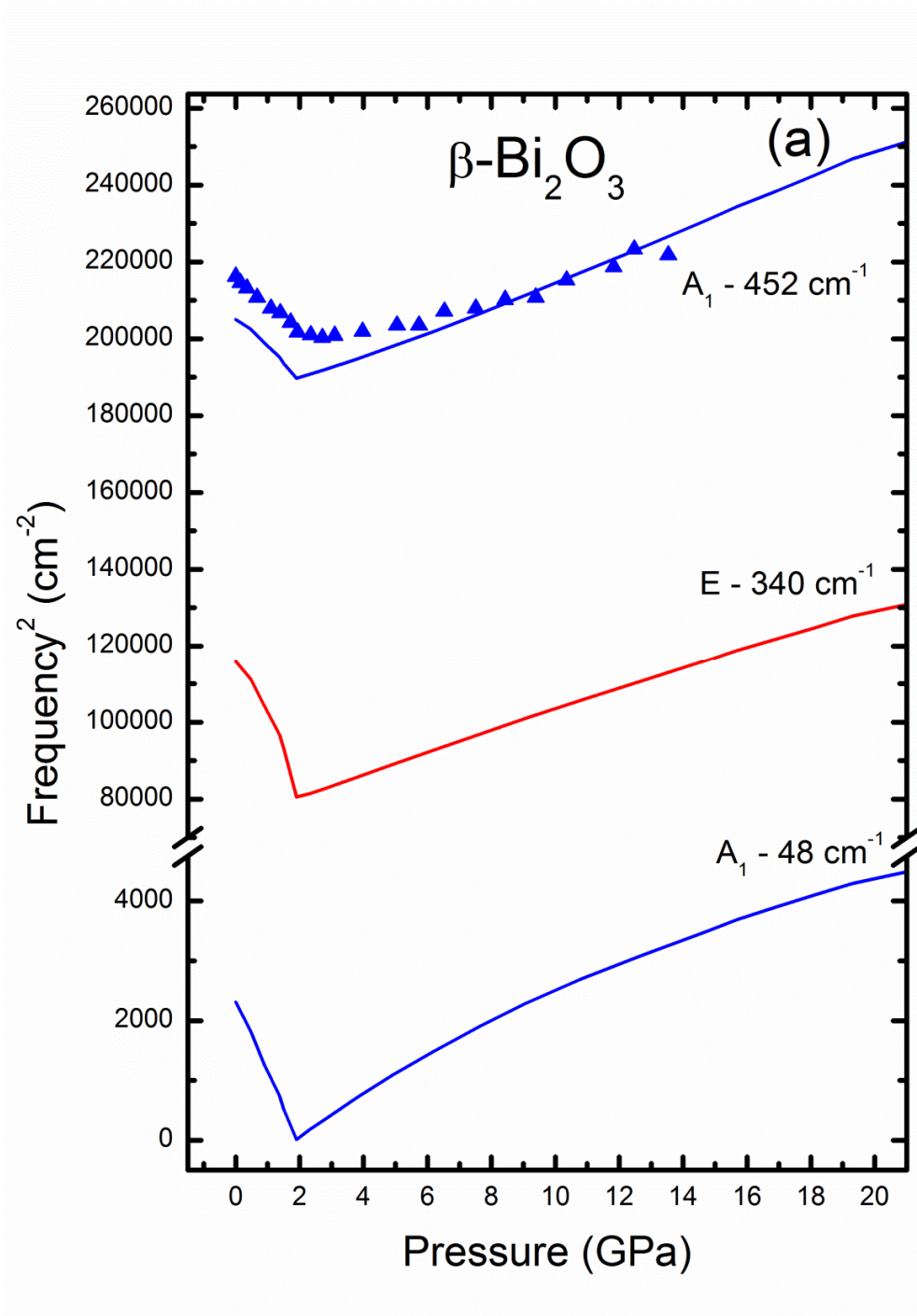
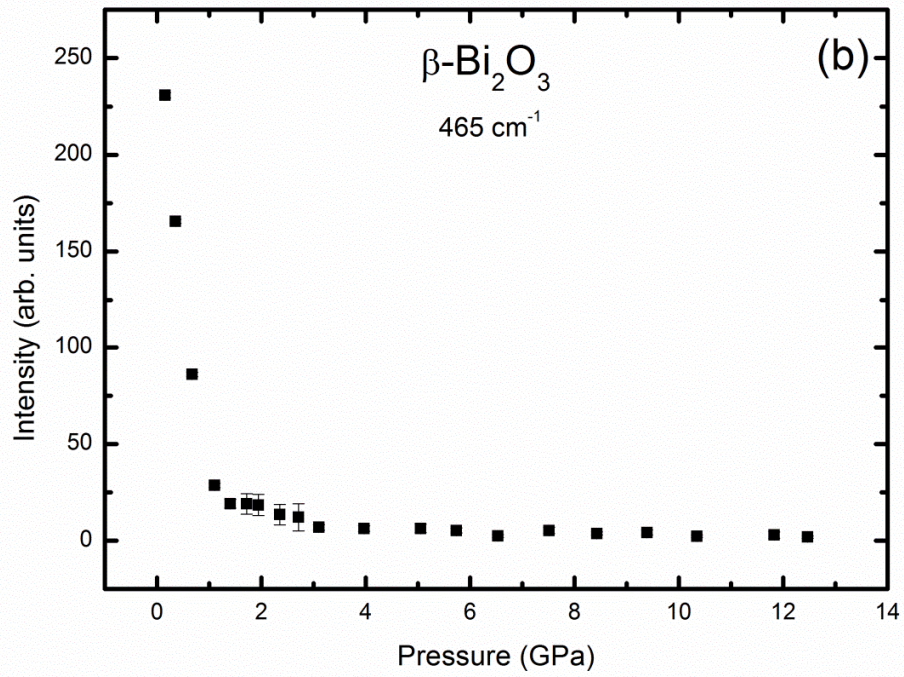


Figure 10



Synopsis TOC

